A COMBINED SUBARU/VLT/MMT 1-5 μm STUDY OF PLANETS ORBITING HR 8799: IMPLICATIONS FOR ATMOSPHERIC PROPERTIES, MASSES, AND FORMATION

Thayne, Curre ; Adam, Burrows ; Itoh, Yoichi ; Matsumura, Soko ; Fukagawa, Misato ; Daniel, Apai ; Nikku, Madhusudhan ; Philip M. Hinz ⋯

(Citation)
The Astrophysical Journal,729(2):128-128

(Issue Date)
2011-03-10

(Resource Type)
journal article

(Version)
Accepted Manuscript

(URL)
https://hdl.handle.net/20.500.14094/90001444

Draft version June 9, 2011
Preprint typeset using LaTeX style emulateapj v. 6/22/04

A COMBINED SUBARU/VLT/MMT 1–5 μM STUDY OF PLANETS ORBITING HR 8799: IMPLICATIONS FOR ATMOSPHERIC PROPERTIES, MASSES, AND FORMATION

Thayne Currie[1], Adam Burrows[2], Yoichi Itoh[3], Soko Matsumura[4], Misato Fukagawa[5], Daniel Apai [6], Nikku Madhusudhan[2], Philip M. Hinz[7], T. J. Rodigas[7], Markus Kasper[8], T-S. Pyo[9], Satoshi Ogino[3]

Draft version June 9, 2011

ABSTRACT

We present new 1–1.25 μm (z and J band) Subaru/IRCS and 2 μm (K band) VLT/NaCo data for HR 8799 and a rereduction of the 3–5 μm MMT/Clio data first presented by Hinz et al. (2010). Our VLT/NaCo data yields a detection of a fourth planet at a projected separation of $\sim$ 15 AU – "HR 8799e". We also report new, albeit weak detections of HR 8799b at 1.03 μm and 3.3 μm. Empirical comparisons to field brown dwarfs show that at least HR 8799b and HR8799c, and possibly HR 8799d, have near-to-mid IR colors/magnitudes significantly discrepant from the L/T dwarf sequence. Standard cloud deck atmosphere models appropriate for brown dwarfs provide only (marginally) statistically meaningful fits to HR 8799b and c for unphysically small radii. Models with thicker cloud layers not present in brown dwarfs reproduce the planets' SEDs far more accurately and without the need for rescaling the planets' radii. Our preliminary modeling suggests that HR 8799b has log(g) = 4–4.5, T_{eff} = 900K, while HR 8799c, d, and (by inference) e have log(g) = 4–4.5, T_{eff} = 1000–1200K. Combining results from planet evolution models and new dynamical stability limits implies that the masses of HR 8799b, c, d, and e are 6–7 M_J, 7–10 M_J, 7–10 M_J and 7–10 M_J. "Patchy" cloud prescriptions may provide even better fits to the data and may lower the estimated surface gravities and masses. Finally, contrary to some recent claims, forming the HR 8799 planets by core accretion is still plausible, although such systems are likely rare.

Subject headings:

1. INTRODUCTION

The HR 8799 planetary system is the first directly imaged multiplanetary system (Marois et al. 2008). Along with Fomalhaut and β Pic, it is also the only imaged system with companion mass ratios and separations reasonably close to the giant planets in the Solar System (Kalas et al. 2008; Lagrange et al. 2009, 2010)[10]. After the initial detection of HR 8799bcd, one or more planets were recovered in prior datasets (Lafreniere et al. 2009; Fukagawa et al. 2009; Metchev et al. 2009). Recently, Marois et al. (2011) imaged a fourth planet – HR 8799e – which we independently detected (see §2).

Mass estimates based on cooling models yield 5–11 M_J for HR 8799b and 7–13 M_J for the other planets (Marois et al. 2008, 2011). Dynamical constraints placed by HR 8799bcd imply that the companions likely have masses below the deuterium-burning limit (Spiegel et al. 2010) and are kept stable by resonant interactions (Fabrycky and Murray-Clay 2010; Moro-Martin et al. 2010). Including the fourth planet, Marois et al. (2011) argue that the planets most likely have masses at the low end of the range allowed by cooling models. With masses of $\approx$ 5–13 M_J, the HR 8799 planets then bridge the gap between the solar system's gas giants/Jupiter-mass planets detected by radial velocity surveys (e.g. Howard et al. 2010) and low-mass brown dwarf companions to nearby stars such as GJ 758B and PZ Tel (Thalmann et al. 2009; Currie et al. 2010; Biller et al. 2010).

Recent studies complicate our understanding of the relationship between brown dwarfs, the gas giants detected in RV surveys, and the HR 8799 planets. The planets' masses are significantly larger than most planets detected by radial velocity and transit methods. Marois et al. (2008) noted that the planets appear slightly redder than the distribution of H/H-K_s colors for old field brown dwarfs. The K-band spectrum of HR 8799b is not well matched by typical L and T-type brown dwarf spectra (Bowler et al. 2010).

Comparisons between the HR 8799 planet photometry/spectroscopy and atmosphere models reveal additional difficulties in understanding their properties within the theoretical framework of standard, cloud deck models that track the field L/T dwarf sequence. In the discovery paper, Marois et al. (2008) briefly mention a discrepancy between temperatures derived from atmosphere models and those estimated from more simple, and presumably most accurate, cooling model estimates. More recently, Bowler et al. (2010) provide a detailed comparison between the HR 8799b spectra and 1.1–4.1 μm photometry and predictions from standard atmosphere models. They show that the 'best-fit' temperatures derived from modeling are inconsistent with cooling model estimates. They also explicitly show that the

[1] NASA-Goddard Space Flight Center
[2] Department of Astrophysical Sciences, Princeton University
[3] Graduate School of Science, Kobe University
[4] Department of Astronomy, University of Maryland-College Park
[5] Department of Earth and Space Science, Graduate School of Science, Osaka University
[6] Space Telescope Science Institute
[7] Steward Observatory, Department of Astronomy, University of Arizona
[8] European Southern Observatory
[9] National Astronomical Observatories of Japan

[10] Here, we consider 1RXJ1609.1-210524b discovered by Lafreniere et al. (2008) to be a more complicated case as its mass ratio and separation are continuous with brown dwarf companions (see Discussion Section)

implied radii for best-fit models are well below the 1.1–1.3 R_J range allowed by standard cooling models (e.g. 0.3–0.5 R_J).

To interpret these modeling difficulties, Bowler et al. (2010) argue that a different atmospheric structure, namely atmospheres with stronger cloud coverage, may better explain the HR 8799b SED. Since atmospheric dust entrained in clouds absorbs more efficiently at shorter wavelengths, photometry for HR 8799b at wavelengths shortward of J band would provide a crucial test of the planet's level of cloud coverage (cf. Burrows et al. 2006). The Bowler et al. (2010) study also found difficulty in reconciling their model fitting of detections from Marois et al. (2008) with 3–5 μm upper limits from Hinz et al. (2010). More sensitive photometry at these wavelengths would then provide better modeling constraints.

In this study, we investigate the atmospheres and dynamics of the HR 8799 planets using new observations obtained at the Subaru Telescope and VLT and a rereduction of MMT data presented by Hinz et al. (2010). Combined with photometry presented by Marois et al. (2008), our data yield nine photometric points spanning 1–5 μm for a detailed comparison to the properties of field brown dwarfs. This wavelength range also provides a sensitive probe of the effects of surface gravity, temperature, (non)equilibrium chemistry, metallicity, and cloud coverage.

We compare the planets' SEDs to atmosphere models exploring a phase space defined by these effects. By quantifying the model fits, we determine the range of parameter space that fails to characterize the planets' SEDs and identify the subset of models that more accurately reproduce the data and may better represent their atmospheres' physical properties. These results will then be used to more thorougly and accurately probe the planets' atmospheric properties in a companion paper (Madhusudhan et al. 2011, in prep.).

Our study is structured as follows. §2 describes our observations, image processing, and detections for each dataset. The first part of §3 compares the HR 8799 planet photometry to the L/T dwarf sequence and the IR properties of other very low-mass objects ($M < 25$ M_J). The rest of §3 presents preliminary comparisons between the HR 8799 planet SEDs and planetary atmosphere models. §4 describes simple dynamical modeling of the system to identify the range of masses for dynamically stable orbits. §5 summarizes our results, discusses our work within the context of previous studies of HR 8799 and planet imaging in general, discusses how our results fit within the context of planet evolution models, and comments on the plausible formation mechanism(s) for the planets.

2. DATA

2.1. *Observations*

Our study combines data from three facilities – VLT/NaCo, Subaru/IRCS, and MMT/Clio – at six broadband filters centered on 1.03 μm to 4.8 μm. The VLT data are the most sensitive and were obtained to place limits on the presence of other candidate planets in the system. The Subaru data at 1.03–1.25 μm were taken to probe the effect of clouds on the planets' atmospheres. Finally, we rereduced the 3–5 μm MMT/Clio data first presented by Hinz et al. (2010) using our reduction pipline, which utilizes advanced image registration, PSF removal, speckle suppression, and flux calibration routines (e.g. LOCI Lafreniere et al. 2007a) also used in Marois et al. (2008).

All of our data were taken in angular differential imaging mode (Marois et al. 2006), where the instrument rotator is adjusted to stay at a fixed angle with respect to the (changing) parallactic angle, resulting in the field of view rotating with time. Combined with the Marois et al. data, we thus have data spanning nine photometric filters that is largely reduced self consistently. Table 1 summarize basic properties of our observations.

2.1.1. *VLT/NaCo K_s band Data*

HR 8799 was imaged with VLT/NaCo on six separate nights in October 2009 as a part of a separate study of the HR 8799 planets (P.I. Daniel Apai; Apai et al. 2011, in prep.). Once publically available, the science and calibration data were downloaded from the ESO VLT archive for October 8–11, nights over which the field rotation for the HR 8799 data was $>$ 30–45 degrees, resulting in a small ($r \sim 0.22$") inner working angle.

The data were taken with the 13.27 mas pixel scale, without coronographic masks, and in pupil tracking mode allowing for angular differential imaging. All data consist of coadded 0.345s exposures totaling $\sim$ 43s a piece and are stored in the standard NaCo datacube format. In this paper, we focus specifically on the October 8 data, which had the highest quality and greatest amount of field rotation. Apai et al. (2011, in prep.) will later present a larger study combining all October 2009 data and Fall 2010 data.

2.1.2. *Subaru/IRCS z(Y) and J band data*

HR 8799 was targeted for direct imaging on August 15, 2009 with the Subaru Telescope using the Infrared Camera and Spectrograph (IRCS; Tokunaga et al. 1998) and AO-188 adaptive optics system in natural guide star mode. The data were taken in the Mauna Kea J band filter ($\sim$ 1.25 μm) and the z filter centered on 1.033 μm, analogous to the better-known Y band filter (e.g. Hillenbrand et al. 2002)[11] During our observations, conditions were photometric with fair natural seeing ($\sim$ 0.65–0.75"). AO-188 yielded a corrected image with FWHM(PSF) $\sim$ 0.06" in z and 0.064" in J. For all observations, the native pixel scale is 20.57 mas/pixel; we used the 0.8" diameter, non-transmissive coronographic mask to block most of the primary starlight.

The z data were taken using 30 second exposures consisting of 6 coadded frames to avoid saturation at separations corresponding to HR8799bcd for a total integration time of 4500s. The J band data consist of 25 second coadded exposures for a total integration time of 1080s. The z data were observed through transit yielding a total field rotation of 172 degrees. The J data were taken about an

[11] The zeropoint wavelength for the z filter listed on the IRCS webpage is 1.033 μm with a width of 0.073 μm. The Y-band filters for comparable cameras are slightly wider but otherwise quite similar: filters for Keck/NIRC (there called "Z"), UKIRT/WFCAM and Gemini/NIRI have zeropoint wavelengths of 1.032, 1.031 and 1.02 μm and widths of 0.156, 0.1 and 0.1 μm, respectively. The IRCS z filter should not be confused with the Sloan z' filter, which covers shorter wavelengths.

hour after transit resulting in very poor field rotation ($\sim$ 6.4 degrees).

2.1.3. *MMT/Clio 3–5 μm Data*

MMT/Clio observations were previously described by Hinz et al. (2010). Briefly, HR 8799 was imaged in three separate observing runs – November 21, 2008, January 10, 2009, and September 12, 2009 – at the L' (3.8 μm) and Barr M (4.8 μm) and a shorter wavelength filter centered on 3.3 μm methane absorption feature and extending from 3.12 μm to 3.53 μm. We focus on the November 2008 and September 2009 runs, which had sufficient field rotation for angular differential imaging. The pixel scale for all Clio data is 48.57 mas/pixel.

The [3.3], L', and M data were imaged for 6780s, 5690s, and 9600s: the total field rotation for data in these three filters was 125.3 degrees, 72 degrees, and 31.8 degrees. While observing conditions for the L' and M data were clear, the [3.3] micron data were taken through variable seeing in two sets between which the AO system failed to yield an acceptable correction.

2.2. *Image Processing/Data Reduction*

2.2.1. *Basic Image Processing and Image Registration*

For our Subaru/IRCS and VLT/NaCo data, we first performed standard dark subtraction, flat fielding, and bad pixel masking. While the NaCo data followed a four-point dither pattern which should wash out image distortion errors, the IRCS data were not dithered. Thus, each IRCS frame was corrected for image distortion using polynomial fits, resulting in a revised pixel scale of 20.53 mas/pixel.

For the MMT/Clio data we then performed sky subtraction. We constructed Clio sky frames from median-combined images obtained for each nod position and subtracted to remove the sky background. Final pixel values for each VLT/NaCo image were nominally constructed from the average pixel value drawn from each frame in the datacube. For regions within 1" of estimated stellar centroid, we determined the average pixel value after iteratively clipping 5σ outliers. For all datasets, bad pixels were identified as outliers within a moving-box median filter, flagged, and interpolated over.

Our image registration procedure closely follows that of Lafreniere et al. (2007b) and Marois et al. (2008). We first copied each image into a larger blank one, coarsely registering them using a priori knowledge about the center of the coronographic mask (for IRCS) or a gaussian fit to a convolved version of the image using the IDL function gcntrd.pro. For precise image registration, we center one image using a 2D cross correlation function relating it to a 180 degree rotation of itself. We then identify the fractional pixel offsets between the reference image and subsequent images yielding the highest correlation. The region of interest used to register IRCS images is focused on diffracted light from the secondary spider. For the Clio and NaCo images we used the non-saturated portions of the stellar PSF, since the diffracted light from the spider is highly suppressed.

2.2.2. *Localized Combination of Images (LOCI) Speckle Supression Processing*

Further data reduction follows the ADI/LOCI reduction procedure described by Lafreniere et al. (2007a) and Marois et al. (2008). We first subtract out the time-independent component of the stellar PSF, exploring two methods. In the first method, we median combine all images for a reference PSF which we subtract from each image, the simple ADI method used by Hinz et al. (2010). In the second method, we construct a two-dimensional radial profile for each image and subtract it to remove the smooth seeing halo.

Next, we perform the LOCI speckle suppression algorithm on the residual images, derotate the processed images and median combine them for a final science image. We compared reductions for a range of LOCI input parameters – dr, N_δ, Na, and geom (see Lafreniere et al. 2007a, for definitions) – to identify the set that maximized the signal-to-noise of the planets, using the set recommended by Lafreniere et al. (2007a) as a starting point. Our pipeline also produces the simple ADI reduction as a byproduct, useful for a separate, sensitive identification of HR 8799b, whose detection in some filters (e.g. [3.3], M) may be more severely limited by photon noise than by speckle noise.

2.3. *Planet Detections and Astrometry*

To identify detected planets in our images, we compute the standard deviation and signal-to-noise ratio of pixel values in concentric annuli (Currie et al. 2010; Thalmann et al. 2009). As a check on our results, we compare our astrometry for candidate detections in a given filter with that obtained by us in other filters and from Marois et al. (2008, 2011) during the Fall 2008 and 2009 epochs. We claim a detection of a planet independent of other datasets if SNR > 5. For SNR = 3–5, the centroid of the candidate planet detection must be the same as that reported for the planet data where SNR > 5 within astrometric errors (typically 0.5 pixels). We centroid the planet using the IDL functions gcntrd.pro and cntrd.pro and adopt a minimum astrometric uncertainty of 0.5 pixels to account for image registration and centroiding/orientation errors. The rightmost column of Table 1 summarizes our planet detections and Table 2 lists their astrometry.

2.3.1. *VLT/NaCo Detections*

Figure 1 shows our reduced VLT/NaCo K_s band image. HR 8799 b and c are detected at better than 25 σ, while HR 8799d is detected at 10 σ. The planets are also free of deep, negative flux troughs at the same separation but slightly different position angles that results from LOCI being applied to datasets with poor field rotation or those where most exposures are taken well before or well after transit (e.g. Marois et al. 2010).

Additionally, our data show a detection of an another point source located interior to and in the same quadrant as HR 8799d consistent with a fourth planet – "HR 8799e". Recently, Marois et al. (2011) announced a multiepoch detection of HR 8799e in K-band and L'-band using Keck/NIRC2. Their detection significance in K-band using Keck/NIRC2 is slightly better than ours ($\sim$ 5 σ vs. our $\sim$ 4 σ). Our photometry using methods described in §2.4 yields an absolute magnitude of $m(K_s) = 12.89 \pm 0.26$, consistent with Marois et al.'s estimate of 12.93 ± 0.22.

Figure 2 compares our astrometry. We measure a centroid position of [E,N] = [-0.306" ± 0.007", -0.217" ± 0.007"], implying a projected separation of 14.8 AU ± 0.4 AU. The average of the August and November 2009 positions from Marois et al. (2011) is [-0.304,-0.203] with an intrinsic uncertainty ∼ 0.01". Our position is then consistent with theirs to within 1.4 σ. Our implied projected physical separation is consistent with Marois et al.'s estimates from multiepoch data: 14.5 AU ± 0.5 AU.

2.3.2. *Subaru/IRCS Detections*

Figure 3 show reduced images at J and z obtained with IRCS. In spite of poor field rotation severely limiting the performance of the ADI/LOCI processing and precluding detectability of objects within ∼ 1", we clearly detect the b planet in our J band data at a ∼ 10 σ significance (top panels). In spite of good seeing conditions, good field rotation, and a 70-minute integration time, we fail to detect any of the planets at a > 5 σ significance in z band (bottom panels). Our reduced image reveals a weak detection of HR 8799b with SNR ∼ 3.7 (bottom-right panel) and a centroid within 0.25 pixels of its centroid in the J-band data obtained one hour later with the same instrument. However, we do not detect HR 8799c or d in our z data. To verify that our low signal-to-noise detection of HR 8799b and nondetections for the other planets do not result from errors in derotation or a jump in parallactic angle near transit[12], we introduced fake planets into each image with a flux equal to ∼ 10 times the local noise of the final image, reran our reduction pipeline separately for frames before and after transit, and recovered their detections.

2.3.3. *MMT/Clio Detections*

Figures 4, 5, and 6 show reduced images obtained with MMT/Clio in the L', [3.3], and M filters. In the L' filter, we detect HR 8799bcd with signal-to-noise higher than that reported by Hinz et al. (2010) and comparable to that obtained in shorter Keck/NIRC2 exposures by Marois et al. (2008). In the [3.3] filter, we detect the c planet at SNR > 5. We marginally detect the b planet at SNR ∼ 3.8. Hinz et al. (2010) formally report a nondetection for b at [3.3] as they adopt a 3σ threshold for detections, though they identify a cluster of pixels ∼ 2.8 σ above the background consistent with b and roughly coincident with our MMT/Clio and VLT/NaCo detections.

Conversely, we do not detect HR 8799d in [3.3], while Hinz et al. (2010) report a low-significance detection. This disagreement is surprising since LOCI greatly improves the planet sensitivity at small separations such as that for the d planet (Lafreniere et al. 2007a). Furthermore, there is a 40mas offset between the reported HR 8799d centroid from Hinz et al. and that from our 10 σ VLT/NaCo detection obtained three weeks later. While their detection is likely instead residual speckle noise, our qualitative conclusion that HR 8799d is very faint at 3.3 μm is consistent with theirs. As with Hinz et al. (2010), we do not detect any of the planets at M band.

[12] For an example of this phenomenon, see http://www2.keck.hawaii.edu/inst/nirc2/vertAngJump.html

2.4. *Photometry for Detections and Upper Limits for Non-Detections*

Photometry for each dataset was performed with IDLPHOT with the aperture radius set to the 0.5×FWHM$_{image}$. In all exposures, the stellar PSF core is either saturated or obscured. For initial photometric calibration, we obtained observations of the stellar primary viewed through a neutral density filter (MMT/Clio, VLT/NaCo) or observed standard stars immediately prior to and after our science exposures (Subaru/IRCS).

Faint companions to stars observed in ADI and processed with LOCI lose flux due to field rotation and self-subtraction. To further calibrate our photometry, we introduce and measure the flux for faint point sources at random position angles over separations encompassing to the HR 8799 planets (0.25"–2") in each registered frame, rerun our ADI/LOCI pipeline, compute the attenuated flux in the final, processed images, and correct for this attenuation. Figure 7 illustrates this flux loss, comparing the input and output flux for fake points sources for our MMT/Clio L' data. While images processed using a simple ADI reduction lose ∼ 20% of their flux, self subtraction is stronger with LOCI, especially at separations less than 0.75". The attenuation curves obtained for data in other filters do not differ qualitatively: LOCI always attenuates more flux than a simple ADI reduction and attenuation is significantly more severe at small separations.

To place limits on our nondetections, we compute 3σ upper limits where we correct our nominal sensitivity limits for point source self-subtraction inherent in ADI/LOCI. The noise is defined in concentric annuli as before, since in most cases (for HR 8799 c and d) radially-dependent speckle noise dominates over radially independent photon noise. Despite using LOCI, our detection upper limit at 3.3 μm for HR 8799d is brighter than the magnitude listed by Hinz et al. (2010). Moreover, our upper limits for HR 8799bcd at M are consistently brighter than those reported by Hinz et al..

In both cases, the disagreement is likely explainable by our correction for point source self subtraction in deriving upper limits from the standard deviation of pixel values. Hinz et al. construct a reference PSF by median-combining all frames and then subtract this reference PSF from each image. For the 3.3 μm data, our reduction pipeline predicts that this processing should attenuate about half of the point source flux at HR 8799d's position[13]. For the M band data, field rotation is poorer and thus self subtraction with this reduction procedure is severe, reaching over 75% at the position of HR 8799d as nearly half the frames are obtained ∼ 3 hours after transit and thus at essentially one position angle. Thus, the gain in sensitivity due to LOCI is reduced by self subtraction, resulting in brighter 3 σ upper limits.

3. PHOTOMETRIC ANALYSIS: CONSTRAINING THE ATMOSPHERIC PROPERTIES OF THE HR 8799 PLANETS

Combining our data with that from Marois et al. (2008) yields planet flux measurements at nine separate

[13] While the total field rotation is large, ∼ 127 degrees, the vast majority of the frames were taken over a time interval with only 30 degrees of field rotation.

wavelengths from 1 to 5 μm. In this section, we use this rich multiwavelength sampling of HR 8799's planet SEDs to provide an empirical comparison with other cool, substellar-mass objects and simple atmospheric modeling constraints on the planets' properties.

3.1. *Near-to-Mid IR Colors of the HR 8799 Planets*

3.1.1. *Methodology*

To compare the near-to-mid IR properties of the HR 8799 planets with those for other cool, substellar objects, we primarily use the sample of L/T dwarfs compiled by Leggett et al. (2010). The L/T dwarf sequence defined by the Leggett et al. sample allows us to determine how the HR 8799 planet SEDs deviate from those for brown dwarfs of similar temperatures. To explore how the HR 8799 planet SEDs compare to those for other planet-mass objects and very low-mass brown dwarfs with T_{eff} = 800-1800K, we include 2M 1207b (5 M_J), 1RXJ1609.1-210524 (9 M_J), AB Pic (13.5 M_J), and HD 203030b ($\sim$ 25 M_J) (Chauvin et al. 2004; Lafreniere et al. 2010; Chauvin et al. 2005; Metchev and Hillenbrand 2006). Table 4 lists photometry for these objects.

We use color-magnitude diagrams constructed from the Y, J, H, K_s, and L' filters to determine whether the HR 8799 planets are similar to or under/overluminous compared to the Leggett L/T dwarf sequence. For simplicity and because there is no published response function for the IRCS z band filter, we treat the IRCS z-band magnitudes/upper limits for the HR 8799 planets as synonymous with its Y-band magnitude.

To provide a physical point of reference for the L/T dwarf sequence and the HR 8799 color-magnitude positions, we overplot loci for standard, chemical equilibrium atmosphere models from Burrows et al. (2006). We specifically choose the Model E case, which assumes that the clouds are confined to a thin layer, where the thickness of the flat part of the cloud encompasses the condensation points of different species with different temperature-pressure intercept points. Above and below the flat portion, the cloud shape function decays to the -6 and -10 power. Thus, above and below the flat portion, the clouds have scale heights $\sim$ 1/7th and 1/11th that of the gas. See Burrows et al. (2006) for more details.

3.1.2. *Results*

Figure 8 shows our color comparisons. At least three of the HR 8799 planets have K_s/K_s-L' positions (upper-left panel) roughly consistent with those for the Leggett L/T dwarf sequence and with 2M 1207b. HR 8799cde have positions overlapping with objects near the L/T dwarf boundary; HR 8799b has a similar K_s-L' color but is underluminous compared to the three other companions and 2M 1207b by a factor of two. It is unclear how its position compares to those for field L/T dwarfs because the sequence is poorly sampled at HR 8799b's K_s band magnitude.

The other three panels of Figure 8 clearly show that HR 8799c, d, and especially b have near-IR colors that depart from the L/T dwarf sequence. In J/J-H and J/J-K_s, the L/T dwarf sequence turns towards blue colors by up to 1.5 mag starting at the L/T transition. While HR 8799c's position is roughly coincident with T0 dwarfs, HR 8799b and d follow an extension of the slope of the L dwarf sequence between J/[J-H,K_s] = 11/[0.6,1.2] and 15/[1.2,2] towards fainter magnitudes and redder colors. HR 8799d's position coincides with that of HD 203030b, while HR 8799b is located closest to 2M 1207b. The H/Y-H color-magnitude diagram shows that HR 8799c also is likely red/underluminous; HR 8799b is 2.5 magnitudes too red in Y-H for its H-band magnitude, indicating that it is underluminous compared to the L/T dwarf sequence at both Y and J.

Figure 8 overplots loci of standard Burrows et al. models for parameters covering a range expected for low-mass, cool brown dwarfs – T_{eff} = 800-1800K, log(g) = 4–5 – and two metallicities (solar and 3$\times$ solar)[14]. With the exception of some L/T dwarf transition objects, the dispersion in color-magnitude positions for L/T dwarfs is well reproduced by model atmosphere loci. This indicates that L/T dwarf atmospheres can be explained within the phase space encompassed by the models' assumed cloud structure and range in temperature, gravity, and metallicity (Burrows et al. 2006).

The HR 8799 planets, especially HR 8799b, are different. They consistently lie below the region enclosed by the standard model atmosphere loci, indicating that their near-IR luminosities are weaker compared to luminosities expected if their cloud structure were well represented by the models. HR 8799b in particular probes a completely different range of parameter space, lying 0.75 magnitudes or more redder than *any* standard atmosphere prediction regardless of temperature. Thus, Figure 8 suggests a strong contrast between the atmospheric properties of L/T dwarfs and the HR 8799 planets.

To summarize, all three HR 8799 planets – especially HR 8799 b – have near-IR colors that cannot be easily understood within the field L/T dwarf sequence. They are consistently red and underluminous at Y and J, indicating that the 1–1.25 μm portion of their SEDs are suppressed in flux. The HR 8799 planets also lie well outside the loci of standard atmosphere models used to interpret the physical properties of L/T dwarfs. Thus, the HR 8799 planet atmospheres are not simply 'scaled down' (in mass) versions of the atmospheres of field brown dwarfs defining the L/T dwarf sequence.

On the other hand, the planets' atmospheres show strong similarity to those for planetary-mass/low-mass brown dwarf companions to nearby stars. Specifically, HR 8799 c and d have similar near-IR colors to HD 203030b, while HR 8799b consistently shows near-IR colors similar to 2M 1207b. The planetary-mass companions 1RXJ1609.1-210524b and AB Pic b are also redder in near-IR colors compared to the L/T dwarf sequence but not underluminous. Within the narrow context of our analysis, planetary-mass companions *in general* might not follow the L/T dwarf sequence.

3.2. *Fiducial Model Atmosphere Fits to the HR 8799 Planet SEDs*

Our color comparisons motivate a further investigation of the HR 8799 planet SEDs to better understand the source of the differences between their near-IR colors and those for field L/T dwarfs. To further explore

[14] We include the 3$\times$ solar models because they produce redder near-IR colors and the HR 8799 planets are red in the near-IR compared to the L/T dwarf sequence.

the physical properties of the HR 8799 planets we compare their photometry to atmospheric models. Because the color-magnitude comparisons indicate that standard model atmospheres provide poor fits to the planet data, we introduce a new set of models to explore additional phase space not covered by the standard models, specifically a different cloud structure:

- **The Burrows et al. (2006) Model A Thick Cloud Layer prescription** – Like the Model E case, this model defines a cloud base at the high temperature interception point with the shape function at higher temperatures/pressures decaying to the -10 power. However, the cloud density tracks the gas density at lower temperatures/pressures ($s_1 = 0$ in their terminology). Thus, clouds in this case are far more extended high in the atmosphere than in the standard Model E case.

  As noted in Burrows et al. (2006), these models are qualitatively similar to the AMES-DUSTY models (Allard et al. 2001). However, they are bluer and brighter than AMES-DUSTY in the near IR because Allard et al. (2001) adopts the interstellar medium particle size distribution. The Model A case fails to reproduce the L/T dwarf sequence as it is consistently too red and underluminous in IR color-magnitude diagrams (Burrows et al. 2006). If the HR 8799 planets have thicker clouds than L/T type brown dwarfs, these models – or some hybrid between them and the "E" models – should reproduce the planets' SEDs far better than the Model "E" case alone.

Changing the cloud prescription radically alters the entire shape of the SED (Figure 9). The K and L' band fluxes are similar. However, the Model A/thick cloud prescription is underluminous over the Y and J passbands by an order of magnitude, underluminous at 1.65 μm by a factor of two but overluminous in the 3.3 μm region covering the trough produced by methane absorption in the Model E cloud prescription. Overall, the Model A SED is much flatter from 1 to 4 μm. Additionally, the Model A prescription washes out the methane absorption feature at 1.65 μm used to identify the L/T dwarf transition (see also discussion in Burrows et al. 2006).

Both the standard models and thick cloud layer models use the formalism described in Burrows et al. (2006) for temperatures T_{eff} = 700–1800 K, gravities with log(g) = 3.75–5, and solar/super-solar abundances of metals. For both models, we assume modal particle sizes of 60 μm–100 μm and a particle size distribution appropriate for clouds (Deirmendjian 1964). For both models we also assume radii from Burrows et al. (1997).

3.2.1. *Fitting Method*

Our atmosphere model fitting follows a simplified version of the fitting procedure employed by Bowler et al. (2010) to model the near-IR spectrum and photometry for HR 8799b. Nominally, we quantify the model fits with the χ^2 statistic,

$$\chi^2 = \sum_{i=0}^{n} (f_{data,i} - F_{model,i})^2 / \sigma^2_{data,i}. \quad (1)$$

We weight each datapoint equally. To account for variability in emission and absolute calibration uncertainties, we set a 0.1 mag floor to σ for each datapoint (see Robitaille et al. 2007). Because of incomplete line lists near the 1.6 μm CH_4 band, we do not compare the models to data at the CH_4l filter (see Bowler et al. 2010; Saumon et al. 2007; Leggett et al. 2007). However, we confirmed that this choice has no consequential bearing on our results.

The z, [3.3], and M photometry include many nondetections. We quantitatively incorporate nondetections in the following way. For model predictions consistent with the 3σ upper limits estimated for each nondetection, we treat the model as perfectly consistent with the data and do not penalize the χ^2 value. For model predictions inconsistent with the 3σ upper limits, we do not automatically discard the model. Rather, we penalize the χ^2 value by determining the flux ratio between the model prediction and the 3 σ upper limit. Specificially, a model prediction 2 and 4 times brighter than the 3 σ upper limit will be contribute 12 (3×4) and 48 (3×16) to the final χ^2 value, respectively.

We fit atmosphere models in two cases. First, to provide a straightforward comparison between our data and the luminosity and colors predicted from atmosphere models we keep the radii fixed to the Burrows et al. (1997) dwarf radii. Second, we vary the radius and identify the scaling factor, $C_k = (R_{scaled}/R_{nominal})$, that minimizes χ^2 for a particular model:

$$C_k^2 = \frac{\sum_{i=0}^{n} f_{data,i} F_{model,i} / \sigma^2_{data,i}}{\sum_{i=0}^{n} F^2_{model,i} / \sigma^2_{data,i}}. \quad (2)$$

We nominally only allow the radius to vary by ± 10% from the assumed Burrows et al. (1997) values to encompass the range of radii for 5–20 M_J objects at 30–300 Myr ($\sim$ 1.1–1.3 R_J).

We determine which models are *formally* consistent with the data by comparing the resulting χ^2 value to that identifying the 3 and 5 σ confidence limits. For the first case, where the planet radius is fixed, the appropriate χ^2 limits are 21.85 and 41.80 for 8 datapoints and seven degrees of freedom. For the second case – a variable planet radius – the limits are 20.1 and 39.4 for 8 datapoints and 6 degrees of freedom.

To select the *best-fit* models, we follow Bowler et al. (2010) by identifying the model with the smallest χ^2 and computing the $\Delta\chi^2$ limit for a 3 σ confidence limit. 'Best-fit' models satisfy χ^2_{model}-$\chi^2_{best} < \chi^2_{99.73\%}$. We do this separately for the Model A and E cloud prescriptions.

3.2.2. *Results for Standard Cloud-Deck Models*

Table 5 summarizes our entire fitting results for models with the standard cloud deck prescription. Figure 10 displays some of these fitting results with the planet radii fixed to the Burrows et al. (1997) values. The top-left panel shows the distribution of χ^2 values for HR 8799b; the top-right panel compares the HR 8799b SED to the 'best-fit' model.

For each planet, the models with the lowest χ^2 values have temperatures within 100K of those derived from

cooling models: T_{eff} = 900K, 1200K, and 1100K for HR 8799b, c, and d (see Marois et al. 2008). Models with a 3× solar abundance of metals have marginally smaller χ^2 values. Adopting the $\Delta\chi^2$ criterion, $\chi^2_{min} + \chi^2_{99.73\%}$, the minimum χ^2 values for modeling b, c, and d are 300.9, 133.2, and 38.9. The range of temperatures and gravities fulfilling this criterion are T_{eff} = 900–1000K, 1100–1300K, 1000–1300K and log(g) = 4.5–5, 4.5–5, and 4–5 for the b, c, and d planets.

However, the fits are quantitatively very poor for HR 8799c and (especially) b. As shown by Figure 10 (top-left panel), the minimum χ^2 value for HR 8799b is a factor of $\sim$ 5.5 times higher than the formal 5 σ confidence limit. The minimum χ^2 value for HR 8799c is twice as large. The large χ^2 difference between that for 'best-fit' models and the formal 5-σ confidence limit suggests that the models do not provide meaningful fits to the data. Fits to the HR 8799d SED are not quite as poor but include only one model with $\chi^2 < \chi^2_{99.73\%}$. Allowing the planetary radii to vary over the range plausible for 5–20 M_J objects does not qualitatively improve the model fits for the b and c planets (Table 5).

The top righthand panel and lower panels of Figure 10 illustrate how the models fail to reproduce the SEDs of HR 8799bcd. For example, for HR 8799b the 'best fit' model provides a good estimate of its K_s band and L' band fluxes and is consistent with its upper limit at M band. At [3.3], however, the model predicts too deep of a trough due to methane absorption, underpredicting the flux by a factor of $\sim$ 3–4. Most strikingly, the model overpredicts the flux at Y and J band *by over an order of magnitude*. The model overestimates the H band and CH_4s flux by a factor of $\sim$ 2. Compared to the best-fitting models, HR 8799c also has too strong of a 3.3 μm flux and too low of a Y band upper limit.

For modeling results discussed in Figure 10, the scaling factors for the radii are almost always C_k =0.9 for temperatures greater than those predicted from cooling models and 1.1 for lower temperatures. To see which radii formally yield the smallest χ^2 values, we allow the radius to vary between 0.2 and 2 times the Burrows et al. (1997) values. The resulting trend of χ^2 vs. T_{eff} for all planets changes, as the minima are systematically pushed towards higher T_{eff} (T_{eff} = 1300–1400 K). However, radius scale factors for the best-fit models imply that the planets are unphysically small – $R_{b,c,d} \sim$ 0.4, 0.6, and 0.7 R_J.

In summary, atmosphere models with standard, cloud deck prescriptions appropriate for brown dwarfs only provide statistically meaningful fits to HR 8799b and c for unrealistically small radii (see also Bowler et al. 2010, for HR 8799b). Assuming radii characteristic of planet-mass objects, we fail to find a single model that provides a statistically meaningful fit to the HR 8799b and c data indicating that such models provide a poor description of the planets' atmospheres (see also Marois et al. 2008; Janson et al. 2010; Hinz et al. 2010). These results are independent of surface gravity for log(g) = 4–5 and whether the planets have solar or 3× solar metallicity. These results then motivate us to see if models with different cloud prescriptions fare better in reproducing the SEDs of HR 8799bcd.

3.2.3. *Results for Thick Cloud Layer Models*

Figure 11 shows and Table 6 summarizes our fitting results for the thick cloud layer models. Best-fit models for the HR 8799 planets cover a similar range in T_{eff} as the standard model fits and cooling model predictions. For HR 8799b, the best-fit model assumes T_{eff} = 900K and log(g)=4.25; the range of best-fit models cover log(g)=4–4.5 and T_{eff} = 900–1000K. The range in log(g) for HR 8799c and d are similar to that for b (log(g)=4.25–4.5 and 4–4.5), whereas their temperatures are slightly higher (1100–1200K and 1000–1200K).

As illustrated by Figure 11, models with thick cloud layers provide *far* better fits to the SEDs of *all three* planets. Quantitatively, the χ^2 minima shrink by factors of 6, 2, and 5 for HR 8799b, c, and d compared to those for Model E fits. For HR 8799b and c, the minima approach the formal 5-σ confidence limit. For HR 8799d, multiple models have χ^2 minima less than the formal 3-σ confidence limit.

The righthand panels of Figure 11 illustrate why the thick cloud layer models are more accurate. For HR 8799b, the best-fit models predict a flat, rising SED from 1 to 1.5 μm, consistent with the planet's weak Y and J band emission. The best-fit models also predict stronger 3.3 μm emission than in the standard model case and in better agreement with HR 8799b's measured [3.3] flux. While the best-fit model for HR 8799c underpredicts its J-band flux while overpredicting its [3.3] and L' band flux, the discrepancies are weaker than in the standard cloud model case. With the exception of the CH_4l filter data, which was not incorporated into our fitting, the best-fit thick cloud model (log(g) = 4.25, T_{eff} = 1100K) for HR 8799d accurately reproduces the planet's flux at every datapoint.

Allowing the planet radii to vary by ± 10% slightly improves the model fits. More importantly, results in more models with χ^2 values below the formal 3σ and 5-σ confidence limits (Figure 12). For these models, the HR 8799b's range of best-fit models have log(g) = 4.25–4.5, and T_{eff} = 900–1000K, and C_k = 0.9–1.02; HR 8799c's have log(g)=4.25–4.5, T_{eff} = 1100–1200K, and C_k = 0.9–0.975; and HR 8799d's have log(g) = 3.75–4.5; T_{eff} = 1000–1200K; and C_k = 0.9–1.09. As before, the scaling factor for each model is correlated with the model's temperature compared to the cooling model estimates.

3.3. *Estimates for "Patchy"/Partly Cloudy Models*

The two models used to fit our data define limiting cases for the cloud structrure in planet atmospheres. The Model A thick cloud layer prescription fits the data for each planet far better. However, intermediate cases – with far thicker clouds than the Model E case but slightly thinner than Model A or a "patchy" cloud coverage – may be more physically realistic. The two processes may be tied together: Ackerman and Marley (2001) show that clouds may become patchy as they sediment below photospheric pressures. Near-IR photometric variability detected from the T2.5 brown dwarf SIMP J013656.5+093347 is consistent with grain free, cloudless regions and grain-bearing cloudy regions rotating in and out of view (Artigau et al. 2009). Cloud patchiness may also be important for defining the L/T dwarf transition (e.g. Marley et al. 2010, and references therein).

We leave a detailed construction of such models to a future paper (Madhusudhan et al., in prep.) but here we qualitatively explore how intermediate cases may affect the predicted planet spectrum (see also Marley et al. 2010). Similar to Burgasser et al. (2002), we follow a highly simplified, crude approach by combining weighted sums of Model A and E cloud prescriptions to approximate an atmosphere whose cloud thickness varies over the seeing disk of the planet[15]. For simplicity, we compare two parameterizations: a "partly cloudy" approximation where we weight the thick cloud model by 60% and a "mostly cloudy" approximation where we weight 90% of the surface by the Model A case.

Figure 13 shows modeling results for these two cases compared against the thick cloud layer results for log(g) = 4 and 4.5. Our approximations yield smaller χ^2 minima for HR 8799b and c; models with partly/mostly cloudy approximations have the smallest χ^2. The best-fit model for HR 8799b has T_{eff} = 900K, consistent with the thick cloud layer model, while temperatures for HR 8799c and d are lower by 100K.

While our approach is entirely ad hoc, it indicates that slightly weakening clouds compared to the limiting Model A case may provide better fits, at least for low surface gravity models (log(g) = 4). Madhusudhan et al. (2011) present a set of new atmosphere models with a range of cloud coverages intermediate between the Model A and E cases to explore how varying the cloud strength between these two extremes affects fits to the data.

4. DYNAMICAL STABILITY ANALYSIS

As shown by Fabrycky and Murray-Clay (2010) and Moro-Martin et al. (2010), stability analysis of the HR 8799 system constrains the planet masses independently of planet cooling and atmospheric modeling. Here, we investigate the plausible mass range of companions imposed by dynamical stability. Later, we will combine the results of these simulations with the implied mass range from atmospheric modeling to identify planet masses consistent with both atmospheric modeling and dynamical stability analysis.

4.1. *Procedure*

Using the Swifter N-body code, an updated version of the Swift package (Duncan et al. 1998), we integrate the equations of motion for the HR 8799 planets. We adopt the Burlirsh-Stoer method to treat close encounters. For all simulations we use an accuracy parameter of 10^{-12} and dynamically evolve the system until one or more planets are ejected or until 100 Myr is reached.

We expand the analysis of Marois et al. (2011) who searched for stable orbital configurations for two sets of planet masses incorporating HR 8799e – 5, 7, 7, and 7 M_J; 7, 10, 10, 10 M_J for b, c, d, and e. We assume a single-2:1 resonance between c and d for the former and a double-2:1 resonance for d-c and c-b pairs for the latter. We hereafter refer to these sets of initial conditions as Cases A and B. To expand upon the Marois et al. (2011) investigation, we considered a wider range of masses for HR 8799bcde – 10, 13, 13, and 13 M_J – with the same double resonance configuration as Case B. We refer to this set of initial conditions as Case C. In all cases, we simply require the system to be stable for 30 Myr – the minimum age of HR 8799 – to be consistent with the data.

We do two sets of 8000 simulations for each case. In the first set, we allow HR 8799e to vary in separation from 13.1 AU to 15.7 AU. This allows us to identify general trends in the time to instability vs. separation for HR 8799e. In the second set, we more finely sample initial orbital properties for the planets assuming a range of 14–15 AU for HR 8799e to better identify stable solutions.

4.2. *Results*

Figure 14 illustrates our simulation results. The top panel displays the time to instability for Case A. The bottom-left and bottom-right panels show the same plot for Cases B and C, respectively. The first set of simulations allowing HR 8799e to range from 13.1 AU to 15.7 AU are shown as orange lines; the second set are shown as black lines.

Our results show that the HR 8799 companions must have masses below the deuterium-burning limit *based on dynamics alone*. Case C configurations are typically only stable for 0.01 Myr and *never* stable for more than 10–20 Myr. Because HR 8799 is a main sequence star, it cannot be as young as 10–20 Myr. Therefore, companion masses for HR 8799cde $\geq$ 13 M_J and a mass for HR 8799b $\geq$ 10 M_J can be ruled out.

Lower planet masses are strongly preferred on dynamical grounds, consistent with the results of Marois et al. (2011). Only seven Case B configurations are stable for $\sim$ 30 Myr, nearly all of which require separations for HR 8799e more than 1-σ different from the position implied by our astrometry. Only two are stable for 100 Myr, and these likewise require anomalously small separations. On the other hand, sixty Case A configurations are stable for 30 Myr. Three are stable for 100 Myr, one of which places HR 8799e at a separation consistent with our astrometry. Our dynamical stability results are in rough agreement with Marois et al. (2011)'s results. They find 12 solutions out of 10^5 possible solutions stable for more than 100 Myr, where HR 8799e varies between 14.35 AU and 14.56 AU. We find 3 out of 1.6×10^4 solutions are stable for 100 Myr over this semimajor axis range.

In summary, we can rule out companion masses greater than 10 M_J for HR 8799b and 13 M_J for the others. The companions cannot be brown dwarfs. Systems with masses of 5 M_J for HR 8799b and 7 M_J for the others are characteristically far more stable than systems with larger masses. We fail to find any stable configuration with 7, 10, 10, and 10 M_J for HR 8799bcde's masses that place HR 8799e at a position consistent with our astometry. While our investigation is not exhaustive, it implies that masses of less than 7 M_J for HR 8799b and less than 10 M_J for the others are most plausible.

5. DISCUSSION

Our primary result in this paper is that the atmospheres of at least two and potentially all of the HR 8799 planets do not easily fit within the empirical IR color

[15] Technically, this is not physically realistic as the temperature-pressure profiles for cloud layer and cloud deck regions would be discontinuous. On the other hand, for a given T_{eff} self-consistent models with intermediate cloudiness (Marley et al. 2010) have color-magnitude positions intermediate between the two extremes, broadly consistent with simple parameterizations (e.g. Burgasser et al. 2002).

sequence for L/T type brown dwarfs of similar temperatures, nor can they be well fit by standard atmosphere models used to infer the properties of brown dwarfs. Adopting realistic assumptions about planet radii, all atmosphere model fits to data for HR 8799b and c are far poorer than any meaningful threshold identifying models consistent with the data. The models primarily fail by underpredicting the 3.3 μm flux and badly overpredicting flux at 1–1.3 μm.

Our analysis suggests that having "thicker" clouds – ones with larger vertical extents – is key to reproducing the planets' SEDs. Compared to cloud structures assumed in standard L/T dwarf atmosphere models, these clouds are more optically thick at a given T_{eff}, so they are visible (in the photosphere) at a lower T_{eff} even though the cloud base is located far below at much higher pressures. Adopting a thick cloud layer prescription, we succeed in identifying models for each planet that quantitatively are good-fitting models. Moreover, the temperatures of these models are consistent with simpler, presumably more accurate cooling model estimates.

5.1. *Comparisons with Previous Studies of HR 8799*

The most direct comparison to this work is the recent analysis of the HR 8799b K-band spectrum and 1.1–4.1 μm photometry from Bowler et al. (2010) whose modeling formalism we largely follow. Bowler et al. (2010) also finds difficulties in using standard atmosphere models to fit HR 8799b's SED and interpret its properties (see also Marois et al. 2008). Likewise, they find that temperatures inferred from standard atmosphere models disagree with cooling model predictions and that the former require unphysically small radii.

Our results indicate that including Y/z band data only exacerbates the already serious disagreement between standard cloud deck model predictions and the planet's SED. Our analysis confirms Bowler et al. (2010)'s inference that HR 8799b's atmosphere is exceptionally dusty compared to field brown dwarfs. Our results extend this inference, indicating that HR 8799c and, plausibly, HR 8799d are also dusty compared to field brown dwarfs.

Janson et al. (2010) noted that while standard atmosphere models – the COND models in their case – can reproduce the mean brightness of HR 8799c's L'-band spectrum they incorrectly predict the spectral slope from 3.9 μm to 4.5 μm. They cite greater atmospheric dust absorption and, especially, non-equilibrium carbon chemistry as features that may bring the models into better agreement. Hinz et al. (2010) argue that incorporating non-equilibrium chemistry is necessary to reproduce the mid-IR photometry of HR 8799bcd since the chemical equilibrium models they use (Saumon et al. 2006) predict M-band fluxes larger than the upper limits they report.

Non-equilibrium carbon chemistry has little effect on the near-IR portion of the SED (e.g. Hubeny and Burrows 2007). Thus, our analysis indicates that thicker clouds – and, by implication, stronger atmospheric dust absorption – are far more important than non-equilibrium chemistry in reproducing the HR 8799 planet 1–5 μm SEDs. Nevertheless, the HR 8799 planet atmospheres are plausibly not in local chemical equilibrium. Since departures from chemical equilibrium alter the spectral structure at 4–5 μm, non-equilibrium chemistry incorporated into thick or "patchy" cloud models may yield better fits to 1–5 μm photometry and mid-IR spectroscopy of the planets. Higher signal-to-noise L' band spectra and detections/more stringent upper limits at M will better identify evidence of non-equilibrium chemistry in the planets' atmospheres.

5.2. *Comparisons with Planet Evolution Models and Implied Masses*

Within the context of the Burrows et al. (1997) planet cooling models, a particular combination of log(g) and T_{eff} defines an object with a mass M and age t. Taking the gravity and temperature range implied by our modeling at face value, we can then identify the mass and age range implied. Our modeling efforts succeed in yielding planets with physically realistic radii. However, if our range of log(g) and T_{eff} were to imply wildly discrepant masses compared to cooling model estimates and dynamical stability requirements or widely varying ages our analysis would have solved one problem only to create comparably serious ones.

Here, we combine all modeling results to identify the range of best-fit parameters and implied parameters – mass and age – from atmosphere models that we consider. We then determine whether the atmospheric and dynamical modeling constraints are consistent and, if so, what mass and age range they imply.

- HR 8799b – The minimum χ^2 value for HR 8799b for thick cloud models is 27.6 if we allow the radius to vary by up to 10% from the Burrows et al. (1997) values and 48.9 if we don't. For the "patchy" cloud approximation, the corresponding χ^2 minima are 20.6 and 51.4. Considering the best-fit models passing the $\Delta\chi^2$ threshold in each case, this range covers log(g) = 4–4.5 and T_{eff} = 800–1000K. Thus, our modeling yields log(g) = 4–4.5, T_{eff} = 800–1000K. Using the Burrows et al. (1997) evolutionary models, this implies a mass and age range of M, t = 5 M_J, 30 Myr to 15 M_J, 300 Myr.

- HR 8799c, d, and e – The minimum χ^2 values here for thick cloud models are 43.5 and 60.7 for c and 5.7 and 5.3 with and without radius rescaling. For the "patchy" cloud approximation, the corresponding χ^2 minima are 14–14.1 for c and 2.8–7.4 for d. For HR 8799c, the range of models passing the $\Delta\chi^2$ threshold for the thick and patchy cloud prescriptions cover log(g) = 4–4.5 and T_{eff} = 1000K–1200K. This yields a mass/age range of 7 M_J, 30 Myr to 15–17.5 M_J at 150–300 Myr. For HR 8799d, the range is log(g) = 3.75–4.5, T_{eff} = 1000-1200K, yielding 5 M_J at 10 Myr to 15–17.5 M_J at 150–300 Myr. Since HR 8799e likely has a bolometric luminosity and K-L colors comparable to HR 8799c and d, its range of masses is plausibly consistent with those derived for HR 8799c and d.

Dynamical constraints require that HR 8799b is less than 7 M_J and HR 8799cde are less than 10 M_J (Section 4 of this work; Marois et al. 2011). The 5 M_J mass estimate for HR 8799d can be ruled out because the primary star is on the main sequence and thus cannot be

10 Myr old. Coupled with the range in surface gravities and temperatures, the implied range in masses are then 6–7 M_J for HR 8799b, 7–10 M_J for HR 8799c, and 7–10 M_J for HR 8799 d. If HR 8799e's atmospheric properties mirror those of c and d, its plausible range of masses is also 7–10 M_J. Conversely, for these ranges of masses, the surface gravities of HR 8799bcde should be no greater than $\log(g) \approx 4.25$.

These estimates are consistent with cooling model estimates from Marois et al. (2008, 2011). For the lower end of the mass ranges, the system age corresponding to these models is ≈ 30 Myr and puts HR 8799's age on the low end of the 30–160 Myr range quoted by Marois et al. (2008). The (disfavored) high end of the mass range corresponds to ~ 100 Myr-old objects.

Despite our success in arriving at self-consistent answers for the planets' masses and ages, we strongly caution against overinterpreting these results. Our results do not *prove* that, above the cloud base, the vertical density/pressure profile of clouds follows that of the gas as a whole (e.g. $s_1 = 0$), as opposed to being truncated at higher pressures. Neither do our results prove that other models with slightly different assumptions about the clouds, grain particles, atmospheric chemistry, etc. provide better fits to the data. In particular, slight modifications to our models may improve the fit at L' band, the datapoint responsible for much of the χ^2 contribution for HR 8799b. Even within the context of our adopted physical models, our sampling in temperature and gravity is also too coarse to precisely estimate best-fit atmosphere parameters.

On the other hand, our analysis provides compelling evidence for thick clouds, motivates future modeling work to test how different assumptions about thick clouds affect model fits to planetary atmospheres, and encourages further observations of substellar objects to test these models. Madhusudhan et al. (2011) will develop and better assess model fits for varying cloud strengths and more precisely and accurately determine temperatures and gravities for the HR 8799 planets and other planetary-mass objects.

5.3. *Constraints On The Formation of the HR 8799 Planetary System*

The planets' large masses and wide orbits make them a particularly interesting probe of planet formation. The favored theory invoked to explain the formation of gas giant planets is *core accretion* (e.g. Mizuno 1980; Pollack et al. 1996; Kenyon and Bromley 2009; Chambers et al. 2010), where cores that have grown to $\approx$ 5–10 $M_\oplus$ rapidly accrete much more massive gaseous envelopes. Alternatively, planets could form by disk instability (Boss 1997, and later papers), where the protoplanetary disk is massive and gravitationally unstable, forming multiple self-gravitating clumps of gas that coalesce into bound, planet-mass objects.

HR 8799's planets are often described as confounding either planet formation model (e.g. Marois et al. 2011) or being clear examples of disk instability-formed planets, as claimed by Dodson-Robinson et al. (2009). They find that cores at distances characterizing the HR 8799 planets cannot reach ~ 10 $M_\oplus$ in mass to undergo runaway gas accretion *even under the most favorable conditions*. They claim that planet-planet scattering cannot create stable, wide-orbit systems like HR 8799's. They conclude that massive, wide-separation gas giants like HR 8799bcd form by disk instability and "can certainly rule out core accretion".

Critical to Dodson-Robinson et al.'s conclusion is their treatment of the core growth rate. The growth rate strongly depends upon the planetsimal approach velocity, which they fix at $v_a = \Omega R_{hill}$. They claim this velocity yields an "optimistically high" growth rate. Their formalism implicitly assumes that planetesimals have an isotropic velocity dispersion ($v_a \sim v_z$), which is valid as long as the scale height of planetesimals accreted by cores (v_z/Ω) is larger than the core's impact parameter, $R_{core}\sqrt{(1+\theta)}$ (Rafikov 2004), where θ is the Safranov number. However, if the planetesimals are dynamically cold such that $v_z \leq \sqrt{p}\Omega R_{Hill}$ (where $p = R_{core}/R_{Hill}$), this condition is violated (Dones and Tremaine 1993; Rafikov 2004). The core can then accrete the entire vertical column of planetesimals at a vastly higher rate since accretion is now essentially two-dimensional (Rafikov 2004).

As a result, Dodson-Robinson et al. (2009) catastrophically underestimate the maximum growth rate by a factor of $p^{-1/2}$, or up to 114, 85, and 68 at the positions of HR 8799b, c, and d (cf. Equations 78, 80, and 82 in Rafikov 2004; see also Rafikov 2010)[16]. Detailed numerical simulations confirm that this rapid growth phase can be reached if collisional fragmentation and gas drag are properly treated (Kenyon and Bromley 2009). The Dodson-Robinson et al. planet-planet scattering simulations also were conducted assuming gas free, planetesimal-free conditions and assumed that planets could not further grow after scattering. However, gas drag and dynamical friction from planetesimals are critically important as they promote orbit circularization and stability (e.g. Goldreich et al. 2004; Ford and Chiang 2007)[17]. Cores with masses sufficient for rapid gas accretion can circularize after being scattered to the outer disk (Bromley and Kenyon 2011, S. Kenyon 2010, pvt. comm.). Simulations by Thommes et al. (in prep.) show that the HR 8799 planet cores could acquire most of their gas *after* scattering.

The mass ratio and semimajor axis distribution of wide planets and low-mass brown dwarfs may help constrain the formation mechanism for HR 8799's planets (Kratter et al. 2010). Core accretion preferentially forms planets with smaller masses and orbital separations, while disk instability has difficulty producing lower-mass gas giants and forming them close to the star (e.g. Rafikov 2005; Kratter et al. 2010). Therefore, if HR 8799bcde formed by core accretion (disk

[16] At first glance, Equation (17) in Rafikov (2010) appears to imply that the limiting distance for core accretion in shear-dominated growth is comparable to Dodson-Robinson et al.'s estimate (44 AU vs. their 20–35 AU). However, Rafikov's result of 44 AU is valid for a Minimum Mass Solar Nebula case (Hayashi 1981). Adopting initial assumptions more comparable to those that Dodson-Robinson et al. assumes – e.g. a disk more massive than the Minimum Mass Solar Nebula or a longer-lived one with $\tau_{disk} =$ 5 Myr instead of 3 Myr– implies that gas giants can in some cases form by core accretion at separations comparable to HR 8799c and b.

[17] In fairness, they clearly acknowledge that their study does not consider planet-planet scattering *in a gaseous disk*, which may result in a more favorable outcome for core accretion.

instability), they should comprise the high-mass extrema (low-mass tail) of a population continuous with radial-velocity detected planets (brown dwarf companions). Using our new results for the masses of the HR 8799 planets, we update Kratter et al.'s plot comparing planet and brown dwarf distributions. We also add the planet-mass companions to 1RXJS1609.1-210524, and 2M J044144b (Todorov et al. 2010, 5–10 M_J, 15 AU); the planet/brown dwarf companion to GSC 06214-00210B (14 M_J, $\sim$ 300 AU Ireland et al. 2010); and the low-mass brown dwarf companion GJ 758B (25–40 M_J, 44 AU Currie et al. 2010).

As shown by Figure 15, the revised masses for the HR 8799 planets and the addition of HR 8799e expand the space between them and brown dwarf companions (asterisks). Visually, they join with the distribution of closer-separation planets plausibly formed by core accretion. The other new companions (red triangles) are continuous with brown dwarfs that may form by disk fragmentation.

While core accretion – especially when coupled with planet-planet scattering – may form the HR 8799 planetary system, HR 8799-like systems are still plausibly uncommon. The Gemini Deep Planetary Survey of 85 nearby, young (mostly solar-mass) stars was typically sensitive to 2 M_J planets at 40–200 AU yet failed to detect any (Lafreniere et al. 2007b). Similarly, non-detections from the deep ($M < 1$ M_J) survey from Kasper et al. (2007) showed that the giant planet populations detected at small separations ($a \lesssim 4$ AU) by RV surveys cannot extend to separations larger than $\sim$ 30 AU. More massive stars like HR 8799 likely have more massive disks, which aid gas giant planet formation. However, their disks also dissipate much more rapidly (Currie et al. 2009): even if critical core masses are reached, the leftover mass of gas may be small. Moreover, rapid core growth results from being able to fragment and then dynamical cool the surrounding planetesimal population. The current state-of-the-art simulations show that this requires Pluto-mass cores to start with (e.g. Kenyon and Bromley 2009), yet the formation time for Pluto-mass objects at wide separations may be long (e.g. Rafikov 2010). Thus, forming HR 8799-like systems by core accretion is difficult, though *not* impossible, and probably happens infrequently.

5.4. *Implications for the Atmospheres of Other Substellar Companions: A Possible Fundamental Difference Between Planetary-Mass Objects and M > 15–20 M_J Brown Dwarfs*

In some ways, the difficulty in reproducing the IR SEDs of the HR 8799 planets mirror difficulties in modeling other planetary-mass objects detected prior to HR 8799bcde. In particular, 2M 1207b also appears discrepant compared to standard atmosphere models as noted in Mohanty et al. (2007) and discussed in this work. Like HR 8799b, 2M 1207b is noticeably underluminous ($\sim$ 2.5 mags) in the near-IR (Mohanty et al. 2007, this work).

To explain 2M 1207b's properties, Mohanty et al. (2007) propose that the object is occulted by an edge-on disk with large, gray dust grains. Alternatively, Mamajek and Meyer (2007) propose that 2M 1207b's properties can be explained as resulting from a recent protoplanet-protoplanet collision. Comparing high-resolution spectra of 2M 1207b to the DUSTY atmosphere models from Allard et al. (2001), Patience et al. (2010) identify a problem similar to that noted for modeling HR 8799b from Bowler et al. (2010) and this work. Namely, allowing the object radius to freely vary yields best-fit radii far smaller ($\approx$ 0.5 R_J) than is physically plausible (cf. Burrows et al. 1997). Patience et al. (2010) also conclude that extinction from an edge-on disk comprised of gray dust grains is also a viable scenario.

For the same reasons – underluminosity/red colors – a disk origin also has been proposed to explain the IR SED of HR 8799b and (to a lesser extent) c and d (Marois et al. 2008). However, Marois et al. (2008) consider the chance alignment of an edge-on circumplanetary disk to be unlikely, especially given that the system is viewed nearly face on. Even more unlikely is the chance that circumplanetary disks or recent protoplanet collisions explain the near-IR properties of two to four separate planets in two systems with very different ages and primary star properties.

Given the success in better reproducing HR 8799bcd's SEDs with thick cloud models and the similarity between HR 8799b and 2M 1207b, it is more plausible that the latter's near-IR spectrum is likewise explained by thick clouds. If this is generally true of planetary-mass objects, thicker clouds may constitute the primary difference between the atmospheres of massive planets and brown dwarfs, at least over the gravity and temperature range enclosed by the HR 8799 planets and 2M 1207b (e.g. log(g) = 3.75–4.5, T_{eff} =900-1600K). Since thicker clouds affect the color-magnitude positions of substellar objects it is quite possible the Model A 'thick cloud' sequence extending to HR 8799b and 2M 1207b from the nominal L/T dwarf boundary continues on to even cooler temperatures (e.g. $T_{eff} \sim$ 700–900K). Since thick clouds present reshape the spectral structure at $\sim$ 1.6 μm (e.g. in the methane band), they may also affect the L/T dwarf transition, which is already known to be dependent upon surface gravity (e.g. Metchev and Hillenbrand 2006; Luhman et al. 2007).

5.5. *Future Work*

Our study motivates the development of a suite of new atmosphere models with clouds intermediate in thickness between the Model E cloud deck and Model A thick cloud layer prescriptions. Adopting these models as fiducial models, we can revisit the (secondary) effects of surface gravity, metallicity, and non-equilibrium chemistry on the atmospheres of planetary mass objects, complementing similar investigations for brown dwarfs (Allard et al. 2001; Marley et al. 2002; Burrows et al. 2006; Hubeny and Burrows 2007). These models will be developed and applied to HR 8799bcde and other planetary-mass objects in upcoming papers (Madhusudhan et al. 2011, in prep.) and may provide a useful comparison to planet parameters derived from cooling models (e.g. Burrows et al. 1997; Baraffe et al. 2003; Fortney et al. 2007, 2008).

New observations at 1–5 μm will provide better constraints on the HR 8799 planet atmospheres. In addition to more sensitive data at Y band and [3.3], Figure 9 (lower-left panel) implies that thick-cloud atmospheres may have *far* stronger emission at $\sim$ 2.3 μm and 3.0 μm than standard models predict. This wave-

length range can be probed for at least HR 8799bcd by current ground-based facilities such as VLT/NaCo, Keck/NIRC2, and MMT/Clio. Integral field spectrographs on *Gemini Planet Imager* (GPI MacIntosh et al. 2008) and SPHERE (Beuzit et al. 2008) will sample the 1–2.5 μm SED region with exceptional sensitivity and thus provide a detailed comparison between observed and predicted atmospheric properties of all planets.

Finally, ongoing collaborations such as the IDPS survey (Marois et al., in progress) and Gemini/NICI (Liu et al. 2010) will better probe the frequency of wide, massive ($\sim$ 5–13 M_J, $>$ 30 AU) around nearby stars. GPI and SPHERE will probe 1–5 M_J planets at even smaller separations (e.g. 5–30 AU). These surveys will produce a far more complete census of Jupiter-mass planets to better determine their ubiquity and constrain how the formation of planets like HR 8799's compare to that expected for lower-mass planets at smaller separations and wide-separation, low-mass brown dwarfs.

We thank the referee, Jonathan Fortney, for a rapid report and suggestions which greatly improved our manuscript. Roman Rafikov, Scott Kenyon, and Ed Thommes provided very detailed, highly informative discussions regarding planet formation by core accretion and planetary dynamics. We also thank Kaitlin Kratter and Ruth Murray-Clay for valuable discussions on the formation of wide-separation planets and brown dwarf companions and for aid in producing our Figure 15. Stanimir Metchev and Marshall Perrin provided useful advice during the beginning stages of this project. Finally, we thank David Lafreniere for numerous conversations regarding the technical details of the ADI/LOCI reduction procedures and for supplying us with some subroutines. TC is supported by a NASA Postdoctoral Fellowship. AB would like to acknowledge support in part under NASA ATP grant NNX07AG80G, HST grant HST-GO-12181.04-A, and JPL/Spitzer Agreements 1417122, 1348668, and 1371432. This work is based in part on on observations made with ESO Telescopes at the Paranal Observatory under programme ID 084.C-656. We acknowledge the significant cultural role and reverence that the Mauna Kea summit has always had within the indigenous Hawaiian community. We are grateful to be able to conduct observations from this mountain.

REFERENCES

Ackerman, A., Marley, M. S., 2001, ApJ, 556, 872
Allard, F., et al., 2001, ApJ, 556, 357
Artigau, E., et al., 2009, ApJ, 701, 1534
Baraffe, I., et al., 2003, A&A, 402, 701
Beuzit, J.-L., et al., 2008, SPIE, 7014, 41
Biller, B., et al., 2007, ApJS, 173, 143
Biller, B., et al., 2010, ApJ, 720, 82L
Boss, A., 1997, Science, 276, 1836
Bowler, B., et al., 2010, ApJ, 723, 850
Bromley, B., Kenyon, S. J., 2011, ApJ submitted
Burgasser, A., et al., 2002, ApJ, 571, 151L
Burrows, A., et al., 1997, ApJ, 491, 856
Burrows, A., et al., 2006, ApJ, 640, 1063
Chambers, J., O'Brien, D., Davis, A., 2010, in Protoplanetary Dust: Astrophysical and Cosmochemical Perspectives, eds.: D. Apai, D. S. Lauretta, 2010, Cambridge University Press
Chauvin, G., et al., 2004, A&A, 425, 29L
Chauvin, G., et al., 2005, A&A, 438, 29L
Chiang, E., et al., 2009, ApJ, 693, 734
Currie, T., Lada, C. J, et al., 2009, ApJ, 698, 1
Currie, T., Bailey, V., Fabrycky, D., Murray-Clay, R., Rodigas, T. J., Hinz, P., 2010, ApJ, 721, 177L
Deirmendjian, D., 1964, Appl. Optics, 3, 187
Dodson-Robinson, S., et al., 2009, ApJ, 707, 79
Dones, L., Tremaine, S., 1993, Icarus, 103, 67
Duncan, M., et al., 1998, AJ, 116, 2067
Fabrycky, D., Murray-Clay, R., 2010, 710, 1408
Ford, E., Chiang, E., 2007, ApJ, 661, 602
Fortney, J. J., Marley, M.S., Barnes, J. W., 2007, ApJ, 659, 1661
Fortney, J. J., et al., 2008, ApJ, 683, 1104
Fukagawa, M., et al., 2009, ApJ, 696, 1L
Goldreich, P., Lithwick, Y., Sa'ari, R., 2004, ARAA, 42, 549
Hayashi, C., 1981, Progress of Theoretical Physics Supplement, 70, 35
Hillenbrand, L., et al., 2002, PASP, 114, 708
Hinz, P., et al., 2006, ApJ, 653, 1486
Hinz, P., et al., 2010, ApJ, 716, 417
Howard, A., et al., 2010, Science, 330, 653
Hubeny, I., Burrows, A., 2007, ApJ, 669, 1248
Ireland, M., et al., 2010, ApJ in press, arXiv:1011.2201
Janson, M., et al., 2010, ApJ, 710, 35L
Kalas, P., et al., 2008, Science, 322, 1345
Kasper, M., Apai, D., Janson, M., Brander, W., 2007, A&A, 472, 321
Kenyon, S. J., Bromley, B., 2009, ApJ, 690, 140L
Kenyon, S. J., Bromley, B., 2010, ApJS, 188, 242
Kratter, K., et al., 2010, ApJ, 710, 1375
Lafreniere, D., et al., 2007a, ApJ, 660, 770
Lafreniere, D., et al., 2007b, ApJ, 670, 1367
Lafreniere, D., et al., 2008, ApJ, 689, 153L
Lafreniere, D., et al., 2009, ApJ, 694, 148L
Lafreniere, D., et al., 2010, ApJ, 719, 497
Lagrange, A.-M., et al., 2009, A&A, 493, 21L
Lagrange, A.-M., et al., 2010, Science, 329, 57
Leggett, S., et al., 2007, ApJ, 667, 537
Leggett, S., et al., 2010, ApJ, 710, 1627
Liu, M., et al., 2010, SPIE, 7736, 53
Luhman, K., et al., 2007, ApJ, 654, 570
MacIntosh, B., et al., 2008, SPIE, 7015, 31
Mamajek, E., Meyer, M., 2007, ApJ, 668, 175L
Marley, M. S., et al., 2002, ApJ, 568, 335
Marley, M. S., et al., 2010, ApJ, 723, 117L
Marois, C., et al., 2006, ApJ, 641, 556
Marois, C., et al., 2007, ApJ, 654, 151L
Marois, C., et al., 2008, Science, 322, 1348
Marois, C., et al., 2010, SPIE, 7736, 52
Marois, C., et al., 2011, Nature, 468, 1080
Masciardi, E., et al., 2005, ApJ, 625, 1004
Metchev, S., Hillenbrand, L. A., 2006, ApJ, 651, 1166
Metchev, S., Marois, C., Zuckerman, B., 2009, ApJ, 705, 204L
Mizuno, H., Prog. Theor. Phys., 64, 544
Mohanty, S., et al., 2007, ApJ, 657, 1064
Moro-Martin, A., Su., K., Rieke, G. H., 2010, ApJ, 721, 199L
Patience, J., et al., 2010, A&A, 517, 76
Pollack, J., et al., 1996, Icarus, 124, 62
Rafikov, R., 2004, AJ, 128, 1348
Rafikov, R., 2005, ApJ, 621, 69L
Rafikov, R., 2010, ApJ in press, arXiv:1004.5139
Robitaille, T., et al., 2007, ApJ, 129, 328
Saumon, D., et al., 2006, ApJ, 647, 552
Saumon, D., et al., 2007, ApJ, 656, 1136
Spiegel, D., et al., 2010, ApJ in press, arXiv:1008.5150
Thalmann, C., et al., 2009, ApJ, 707, 123L
Todorov, K., Luhman, K., McCleod, B., 2010, ApJ, 714, 84L
Tokunaga, A., et al., 1998, SPIE, 3354, 512
Zuckerman, B., Song, I., 2009, A&A, 493, 1149

TABLE 1
OBSERVATIONS

Telescope/Instrument	Filter	Date	Exposure Time (s)	Field Rotation (degrees)	Detections
MMT/CLIO	L'	November 21, 2008	5460	83.88	b, c, d
	M	November 21, 2008	9600	31.8	–
	[3.3]	September 12, 2009	6780	128.53	b[1], c
Subaru/IRCS	z	August 15, 2009	4200	172	b[1]
	J	August 15, 2009	1080	7.4	b
VLT/NaCo	K_s	October 8, 2009	6185	63	b, c, d, e

NOTE. — Note (1) – Companion has a low signal-to-noise detection because it is intrinsically faint (photon-noise dominated region).

TABLE 2
ASTROMETRY (E["], N["] POSITION)

Date	11-21-2008	8-15-2009	9-12-2009	10-8-2009
Planet				
HR 8799b	1.532 ± 0.02, 0.796 ± 0.02	1.536 ± 0.01, 0.785 ± 0.01	1.538 ± 0.03, 0.777 ± 0.03	1.532 ± 0.007, 0.783 ± 0.007
HR 8799c	-0.654 ± 0.02, 0.700 ± 0.02	-	-0.634 ± 0.03, 0.697 ± 0.03	-0.627 ± 0.007, 0.716 ± 0.007
HR 8799d	-0.217 ± 0.02, -0.608 ± 0.02	-	-	-0.241 ± 0.007, -0.586 ± 0.007
HR 8799e	-	-	-	-0.306 ± 0.007, -0.217 ± 0.007

NOTE. — The 8-15-2009 astrometry listed for HR 8799b comes from the J band data because this data yields a higher signal-to-noise detection.

TABLE 3
PHOTOMETRY

Filter	z	J	H	$CH4_S$	$CH4_L$	K_s	[3.3]	L'	M
λ (μm)	1.03	1.248	1.633	1.592	1.681	2.146	3.3	3.776	4.8
Planet									
b	18.24 ± 0.29	16.52 ± 0.14	14.87 ± 0.17	15.18 ± 0.17	14.89 ± 0.18	14.05 ± 0.08	13.96 ± 0.28	12.68 ± 0.12	> 11.37
c	> 16.48	14.65 ± 0.17	13.93 ± 0.17	14.25 ± 0.19	13.90 ± 0.19	13.13 ± 0.08	12.64 ± 0.20	11.83 ± 0.07	> 11.22
d	> 15.03	15.26 ± 0.43	13.86 ± 0.22	14.03 ± 0.30	14.57 ± 0.23	13.11 ± 0.12	> 11.63	11.50 ± 0.12	> 11.15
e						12.89 ± 0.26		11.61 ± 0.12	

NOTE. — Magnitudes listed are the *absolute magnitude* of the companions, assuming a distance of 39.4 pc. (1) H, CH4S, CH4L, and K band photometry for HR 8799bcd taken from (Marois et al. 2008). J band photometry for HR 8799c and d also taken from Marois et al. (2008). L' band (3.8 μm) photometry for HR 8799e taken from Marois et al. (2011). Photometry/upper limits at 3.3 μm, L' band and M band (4.8 μm) for HR 8799bcd are taken from this work.

TABLE 4
ADOPTED PHOTOMETRY FOR OTHER PLANET-MASS OBJECTS AND LOW-MASS BROWN DWARFS

Companion	D (pc)	J	H	K	L'	References
2M 1207b	52.4	16.40 ± 0.2	14.49 ± 0.21	13.33 ± 0.11	11.68 ± 0.14	1,2
1RXJ1609.1-210524	140	12.17 ± 0.12	11.139 ± 0.07	10.44 ± 0.18	9.14 ± 0.3	3,4
AB Pic b	47.3	12.80 ± 0.10	11.31 ± 0.10	10.76 ± 0.08	-99	5
HD 203030b	40.8	15.08 ± 0.55	13.80 ± 0.12	13.16 ± 0.10	-99	6

NOTE. — All magnitudes listed are absolute magnitudes. References – 1) Chauvin et al. (2004), 2) Mohanty et al. (2007), 3) Lafreniere et al. (2008), 4) Ireland et al. (2010), 5) Chauvin et al. (2005), 6) Metchev and Hillenbrand (2006).

TABLE 5
STANDARD MODEL (MODEL E) FITTING RESULTS

Model Run	χ^2_{min}	log(g), T_{eff} (for χ^2_{min})	C_k	$\Delta\chi^2$	log(g), log(T_{eff}) ($\chi^2 < \Delta\chi^2$)
HR 8799b					
Model E solar, 3x	279.0	4.5, 900K	1	291.85	4.5–5, 900–1000K
Model E solar, 3x (C_k = 0.9–1.1)	264.5	4.5, 900K	0.91	286.4	4.5, 900K; 5, 1000K
Model E solar, 3x (C_k=0.2–2)	36.6	4.5, 1400	0.34	58.5	4, 1400K; 4.5, 1300–1500K; 5, 1400K
HR 8799c					
Model E solar, 3x	120.8	5, 1200K	1	142.7	4.5, 1100K; 5, 1200K–1300K
Model E solar, 3x (C_k=0.9–1.1)	71.0	5.0, 1300K	0.9	92.5	5, 1300K
Model E solar, 3x (C_k=0.2–2)	17.6	4.5, 1400	0.54	39.5	4, 1300-1700K; 4.5, 1300–1700K; 5, 1400–1700K
HR 8799d					
Model E solar, 3x	17.0	4.5, 1100K	1	38.5	4.5, 1100K; 5, 1200K
Model E solar, 3x (C_k=0.9–1.1)	17.0	4.5, 1100K	0.9	38.5	4.5, 1100-1200K; 5, 1200–1300K
Model E solar, 3x (C_k=0.2–2)	10.91	4.5, 1300K	0.64	32.8	4, 1300–1600K; 4.5, 900—1700K; 5, 1200–1700K

NOTE. — Where the metal rich models are considered (first three rows for each planet), they always provide the smallest χ^2 value.

TABLE 6
THICK CLOUD MODEL (MODEL A) AND "PATCHY" CLOUD APPROXIMATION FITTING RESULTS

Model Run	χ^2_{min}	log(g), T_{eff} (for χ^2_{min})	C_k	$\Delta\chi^2$	log(g), log(T_{eff}) ($\chi^2 < \Delta\chi^2$)
HR 8799b					
Model A solar	48.9	4.25, 900K	1	70.8	4, 900K; 4.25, 900K; 4.5, 900-1000K
Model A solar (C_k=0.9–1.1)	27.6	4.5, 1000K	0.9	47.7	4, 900K; 4.25, 900K; 4.5, 900-1000K
Model A/E solar (60% thick clouds)	91.5	4, 900K	1	111.6	4, 800K
Model A/E solar (60% thick clouds, C_k=0.9–1.1)	85.5	4, 900K	1	105.6	4, 800–900K
Model A/E solar (90% thick clouds)	51.4	4, 900K	1	71.5	4, 800-900K
Model A/E solar (90% thick clouds, C_k=0.9–1.1)	20.6	4, 900K	1	40.7	4, 800–900K
HR 8799c					
Model A solar	60.7	4.5, 1100K	1	82.6	4.25, 1100K; 4.25, 1100K 4.5, 1100K–1200K
Model A solar (C_k=0.9–1.1)	43.5	4.5 1200K	0.9	63.6	4.25, 1100K; 4.5, 1100-1200K
Model A solar (60% thick clouds)	14.1	4, 1000K	1	34.5	4, 1000K
Model A solar (60% thick clouds, C_k=0.9–1.1)	14.0	4, 1000K	1	34.1	4, 1000-1100K
Model A solar (90% thick clouds)	51.6	4, 1000K	1	71.7	4, 1000K
Model A solar (90% thick clouds, C_k=0.9–1.1)	48.0	4, 1100K	1	68.1	4, 1000-1100K
HR 8799d					
Model A solar	5.7	4.25, 1100K	1	25.8	3.75, 1000K; 4, 1000-1100K 4.25, 1100K; 4.5, 1100-1200K
Model A solar (C_k=0.9–1.1)	5.3	4.5, 1200K	0.98	27.2	3.75–4, 1000-1100K; 4.25, 1000-1200K 4.5, 1100-1200K
Model A solar (60% thick clouds)	7.4	4, 1000K	1	27.5	4, 1000-1100K
Model A solar (60% thick clouds, C_k=0.9–1.1)	2.8	4, 1000K	1	22.9	4, 1000-1100K
Model A solar (90% thick clouds)	8.8	4, 1000K	1	28.9	4, 1000-1100K
Model A solar (90% thick clouds, C_k=0.9–1.1)	3.1	4, 1000K	1	23.2	4, 1000-1100K

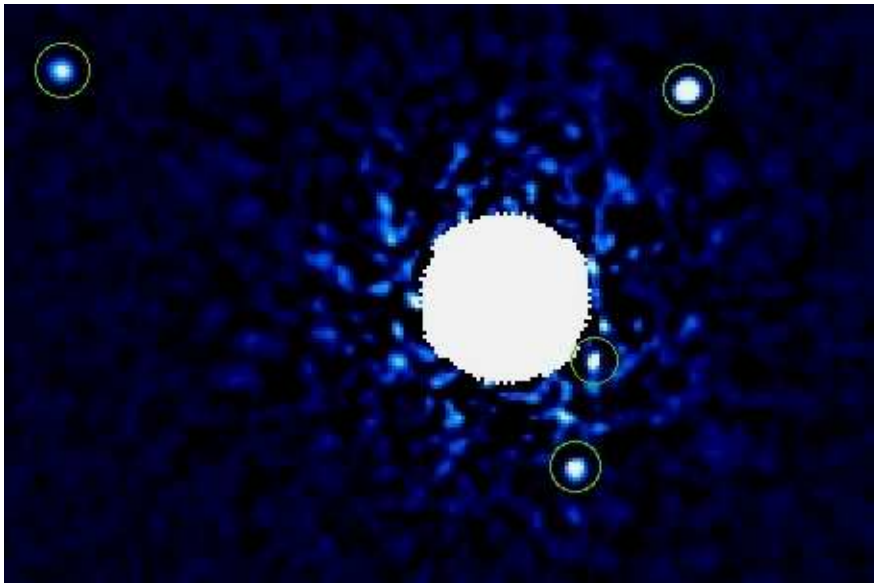

FIG. 1.— VLT/NaCo image of the HR 8799 planetary system. Previously detected planets – HR 8799b, c, and d – are easily visible at high signal-to-noise. At ~ 0.375" separation, we detect an additional object consistent with being a fourth planet orbiting HR 8799 – HR 8799e. This same object was independently detected by Marois et al. (2011) and confirmed to be a fourth planet. HR 8799e (and d, to a lesser extent) appear slightly smaller than b and c because of point source self subtraction inherent in LOCI processing.

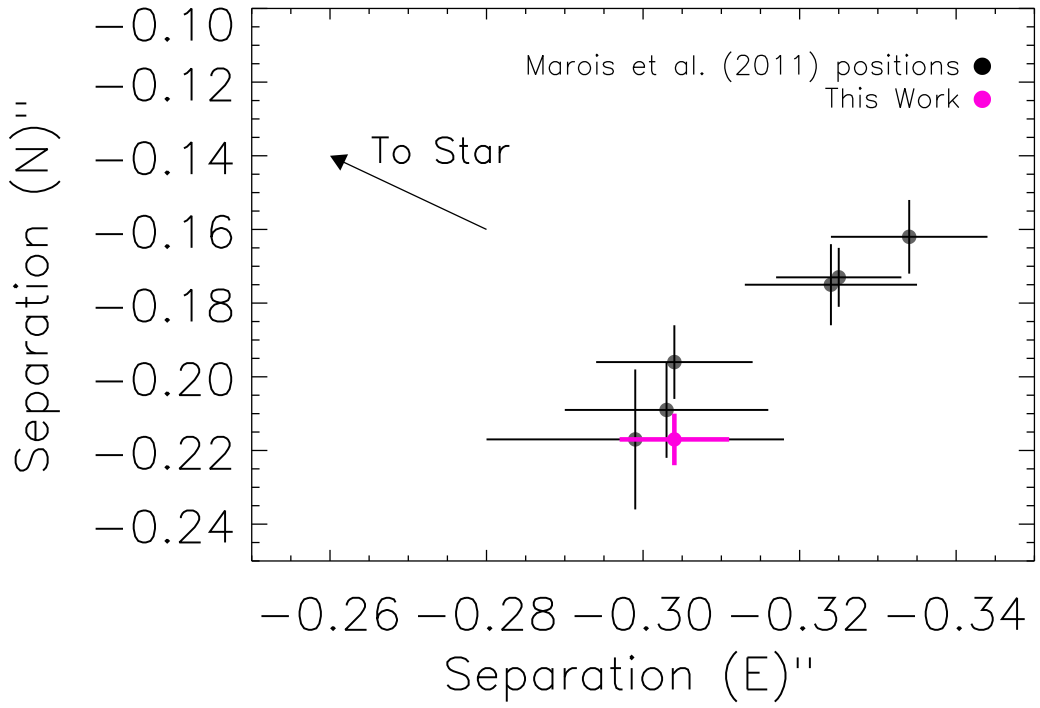

FIG. 2.— Astrometry for HR 8799e comparing positions from Marois et al. (2011) and from our work. The arrow identifies the direction to the HR 8799 primary. The two points from Marois et al. (2011) nearest to our October 8, 2009 measurement were taken in August 2009 and November 2009, respectively. Our astrometry are consistent with those from Marois et al. (2011) within errors.

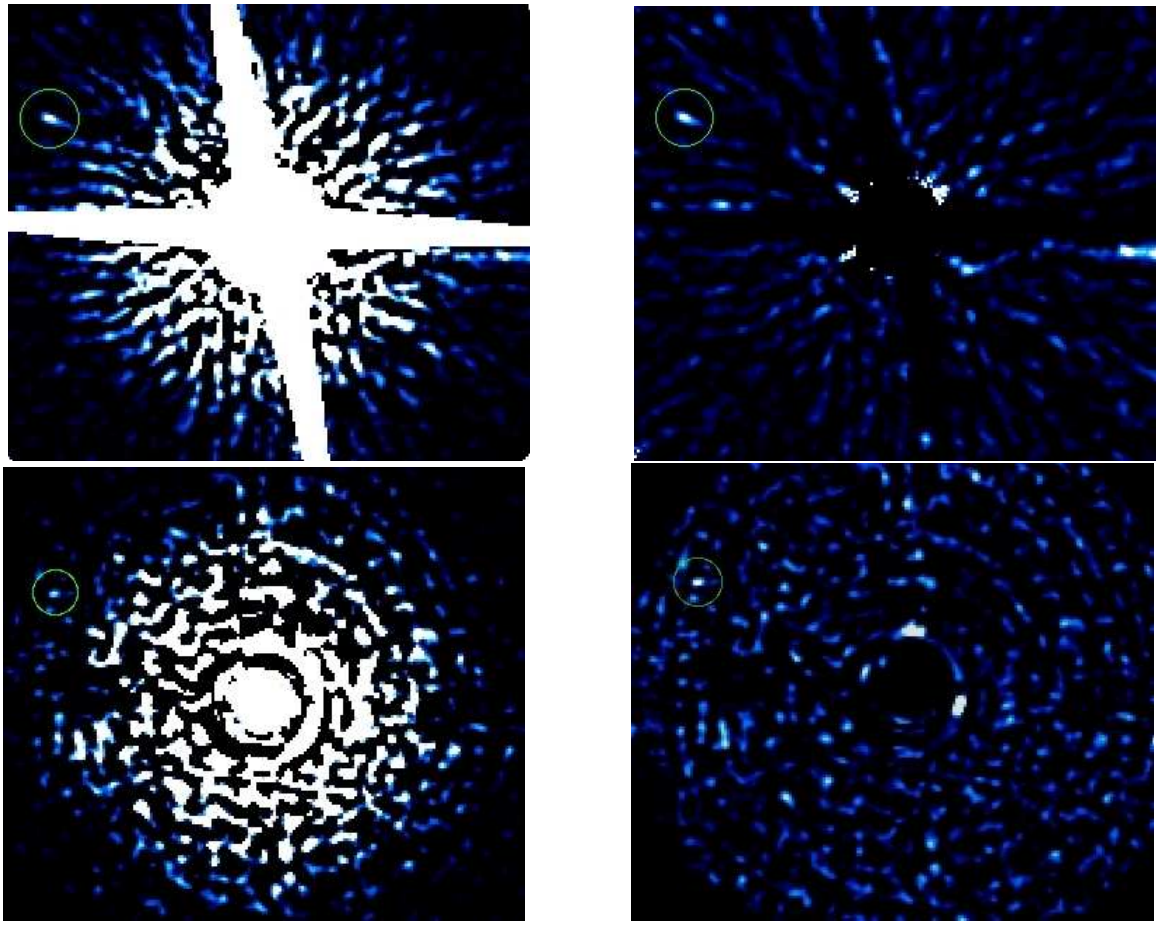

FIG. 3.— Subaru/IRCS images (left panels) and signal-to-noise maps (right panels) obtained at J band (top panels) and z band (bottom panels). The poor field rotation and short integration time in J limit our detection to HR 8799b. Despite over an hour of integration time in z band, we marginally detect HR 8799b but fail to detect the other planets.

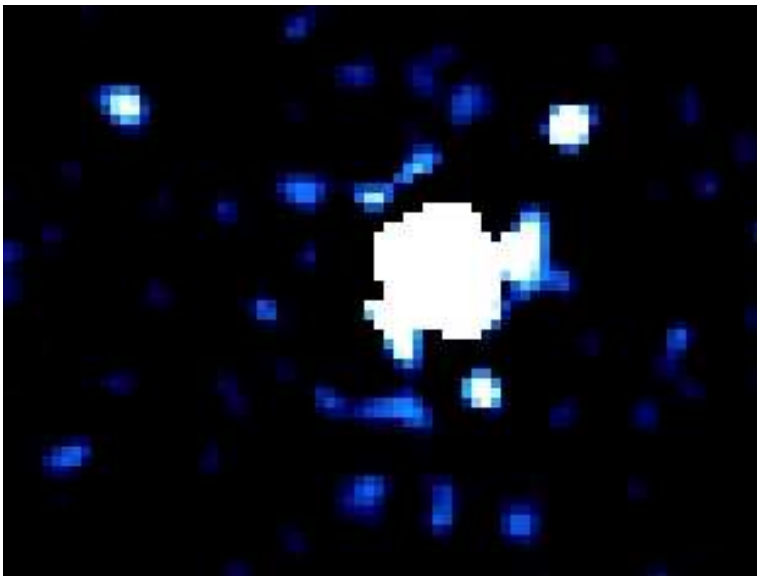

FIG. 4.— MMT/Clio image of the HR 8799 system at L'/3.8 μm. The three planets are clearly visible and all are detected at SNR > 5.

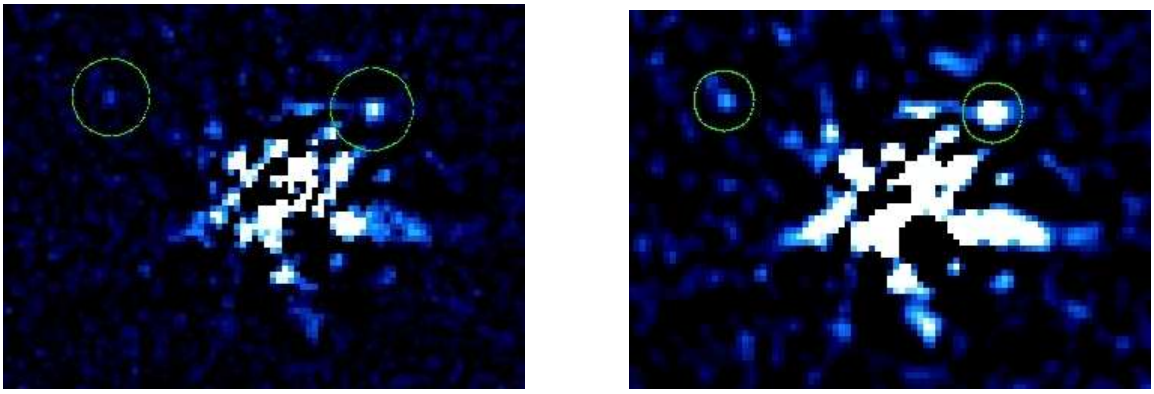

FIG. 5.— MMT/Clio image at 3.3 μm. (Left panel) The image shown with a high dynamic range to more clearly show the detection of HR 8799c. (Right panel) The image with a smaller dynamic range to better illustrate the marginal detection of HR 8799b.

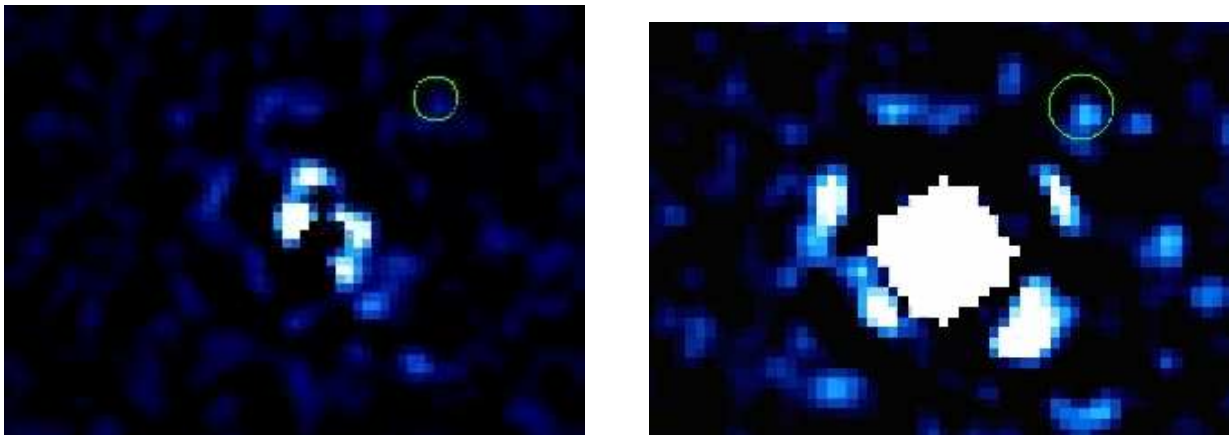

FIG. 6.— MMT/Clio image at M'/4.8 μm shown with slightly different procedures for PSF subtraction (left panel, simple ADI reduction; right panel, radial profile subtraction with LOCI reduction) and different dynamic ranges (left panel, high dynamic range; right panel, low dynamic range to show residual noise). The circle identifies the centroid position of HR 8799c in the L' image obtained on the same night. While a local peak appears near the position of HR 8799c, we do not identify any $> 3\text{-}\sigma$ peaks consistent with any of the planets in these images.

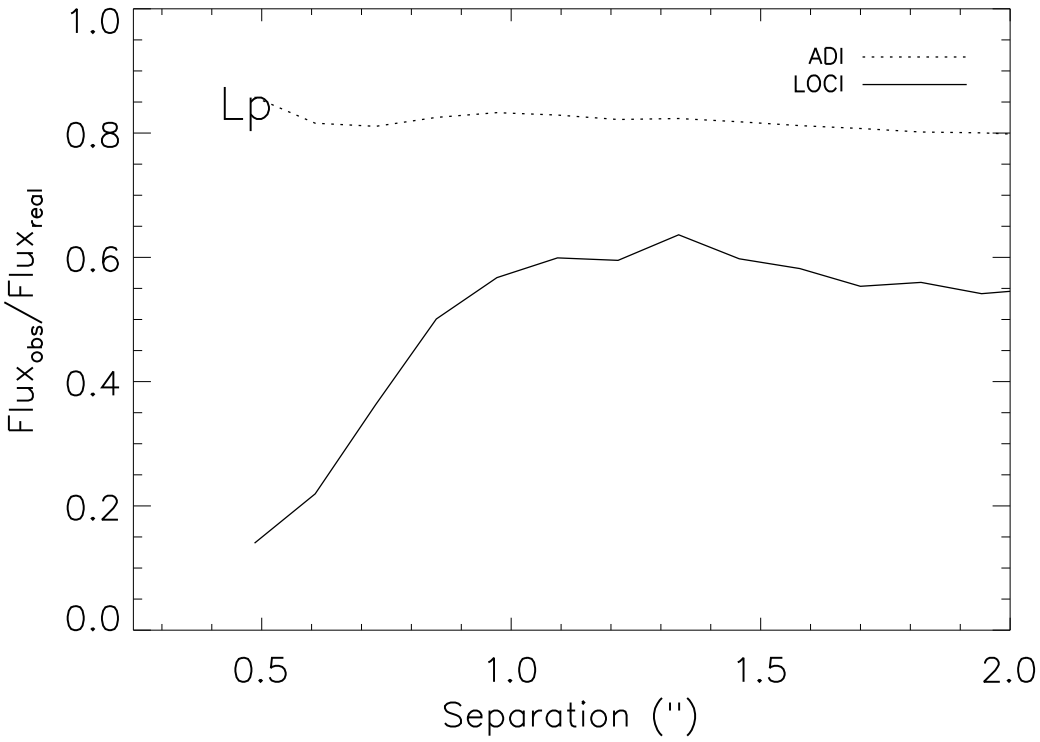

FIG. 7.— Plot of the point source self subtraction for LOCI as a function of separation for our MMT/Clio data for a simple ADI reduction and our LOCI reduction. LOCI attenuates more flux, especially interior to 0.75".

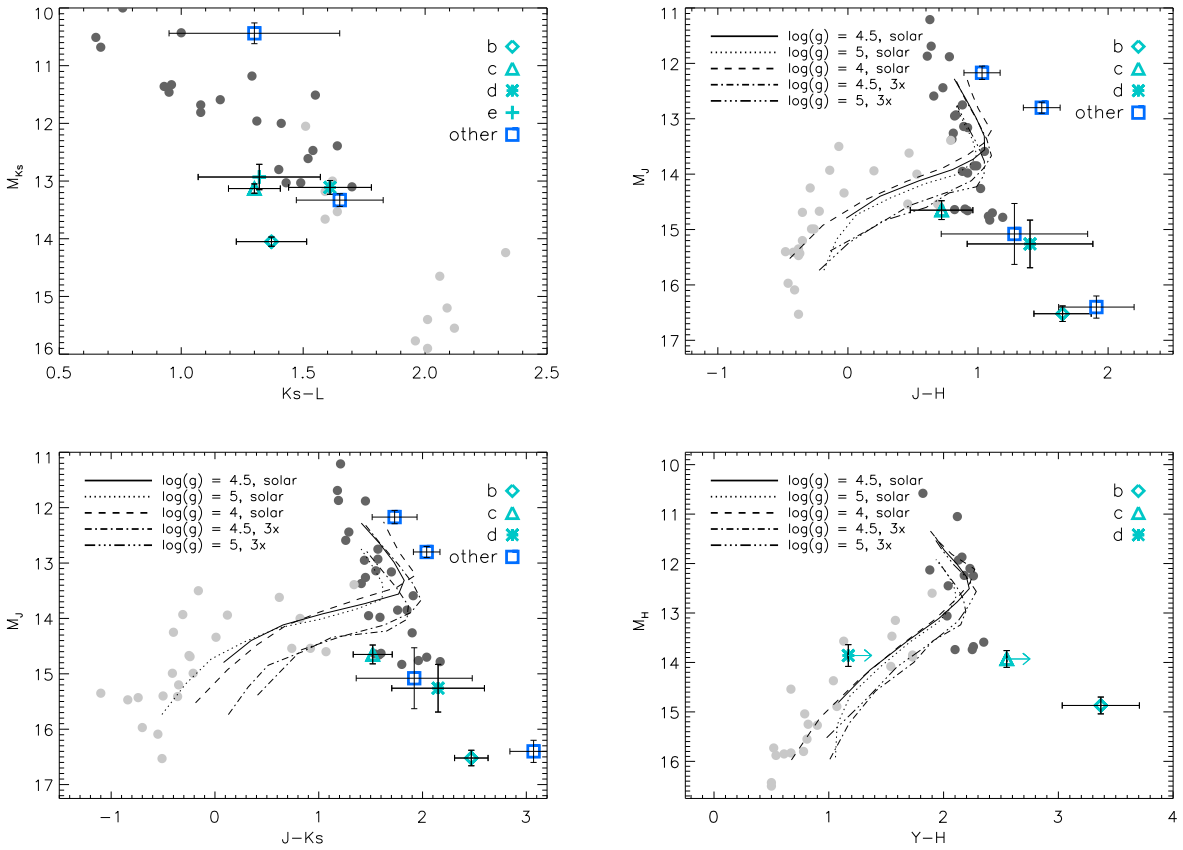

FIG. 8.— Color-magnitude diagrams comparing the HR 8799 planets with field L dwarfs (black dots) and T dwarfs (grey dots) and other planetary or very low-mass brown dwarf companions (squares). In K_s/K_s-L' (top-left panel), the planets follow the L/T dwarf sequence. In at least one of the diagrams including Y, J, and H-band data (top-right panel; bottom panels), the planets are red/underluminous compared to the empirical L/T dwarf sequence and the synthetic L/T dwarf colors from Burrows et al. (2006) for a range of metallicities and gravities. The positions for other planetary-mass/low-mass brown dwarf companions also depart from the L/T dwarf sequence, especially 2M 1207b.

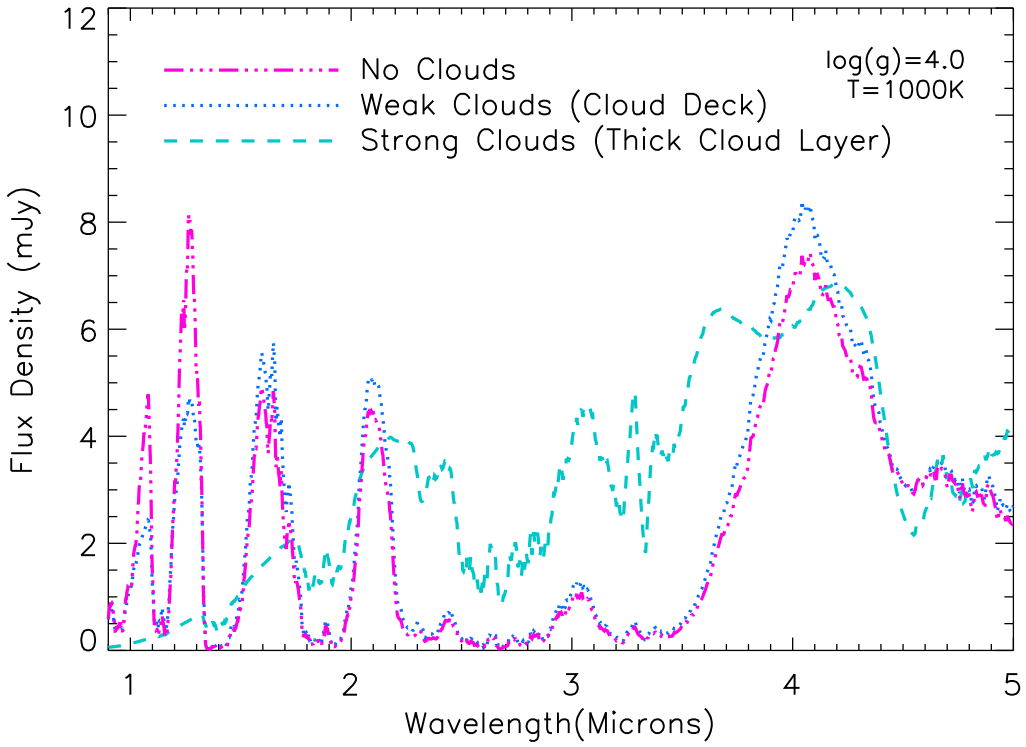

FIG. 9.— Comparing SEDs for different cloud prescriptions (no clouds, Model E, and Model A) at a given temperature and gravity.

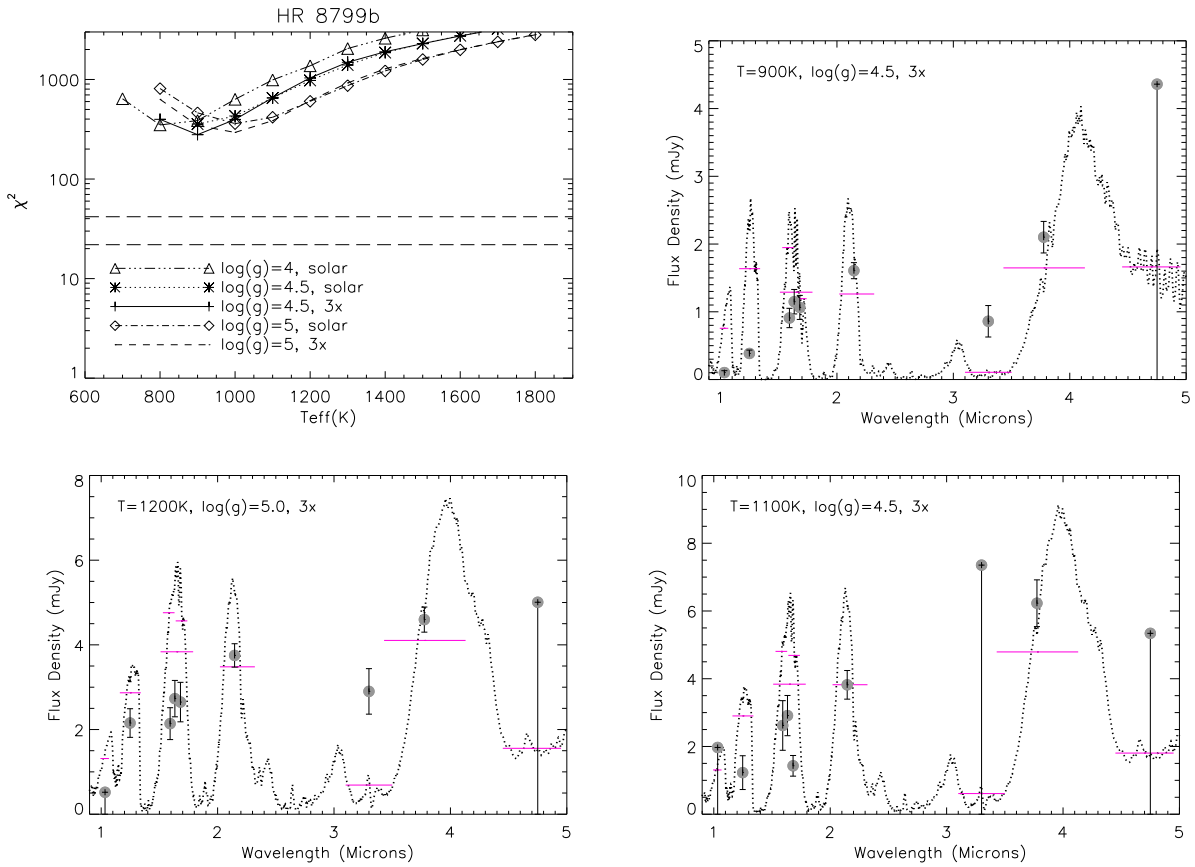

FIG. 10.— Fitting results for the standard cloud deck models assuming the Burrows et al. (1997) radii. The top-left panel show the distribution of χ^2 vs. T_{eff} for model fits to HR 8799b with a range of surface gravity and metallicity. The top-right panel compares the HR 8799b planet SED to the model with the smallest χ^2 value. The bottom panels compare the HR 8799c (left) and HR 8799d (right) SEDs to the best-fit models for these data. In the SED comparisons, the horizontal magenta lines identify the flux of the model in the photometric filters convolved over the filter function. The width of the magenta line corresponds to the width of the filter.

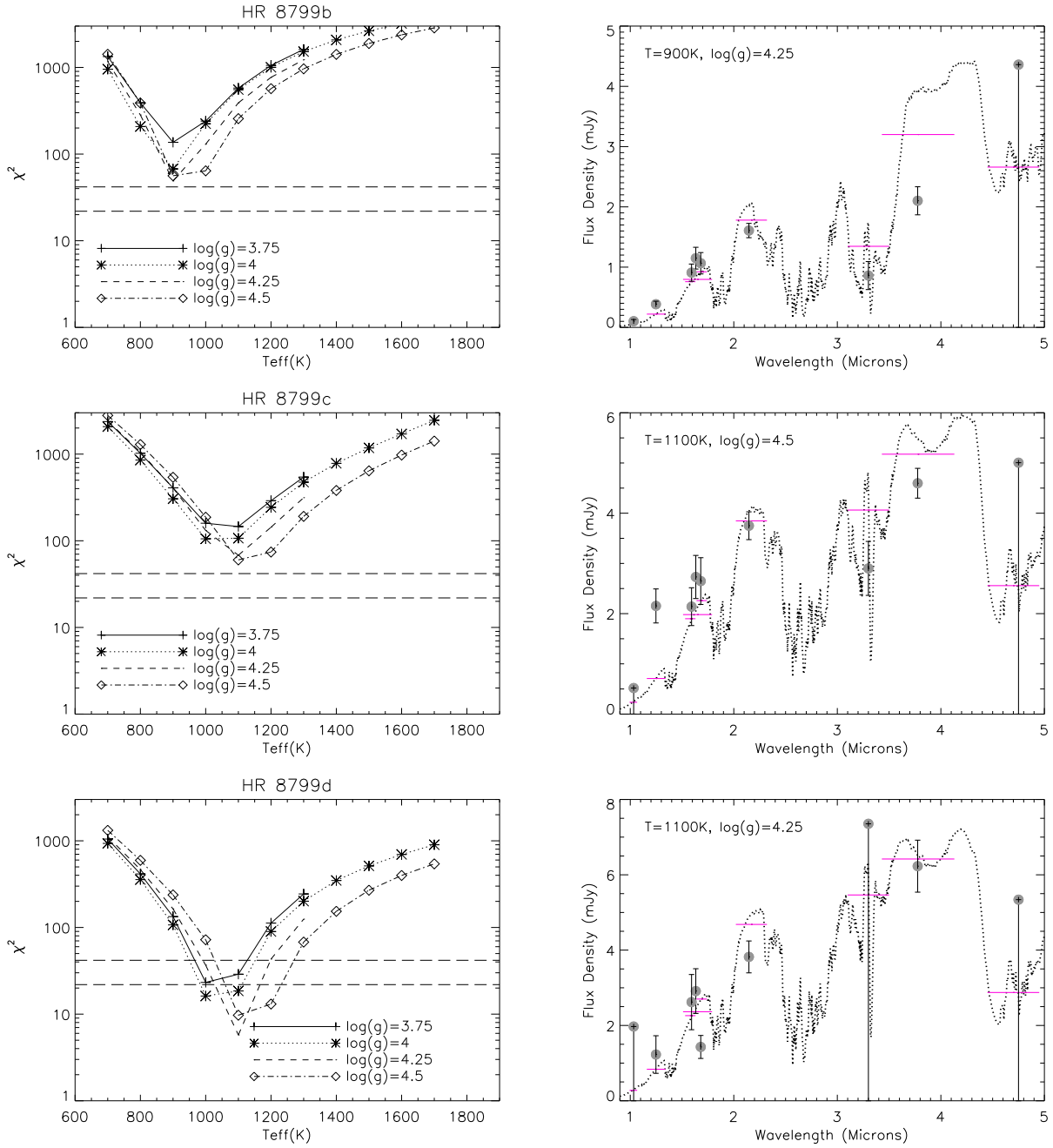

FIG. 11.— Fitting results for the Model A, thick cloud layer prescription with a modal particle size of 60 μm. The lefthand panels show the χ^2 distributions for each planet while the righthand panels compare the planet SEDs to the best-fit models in each case. Compared to the Model E, standard cloud deck fits, these models yielded smaller χ^2 minima and better fits to the data.

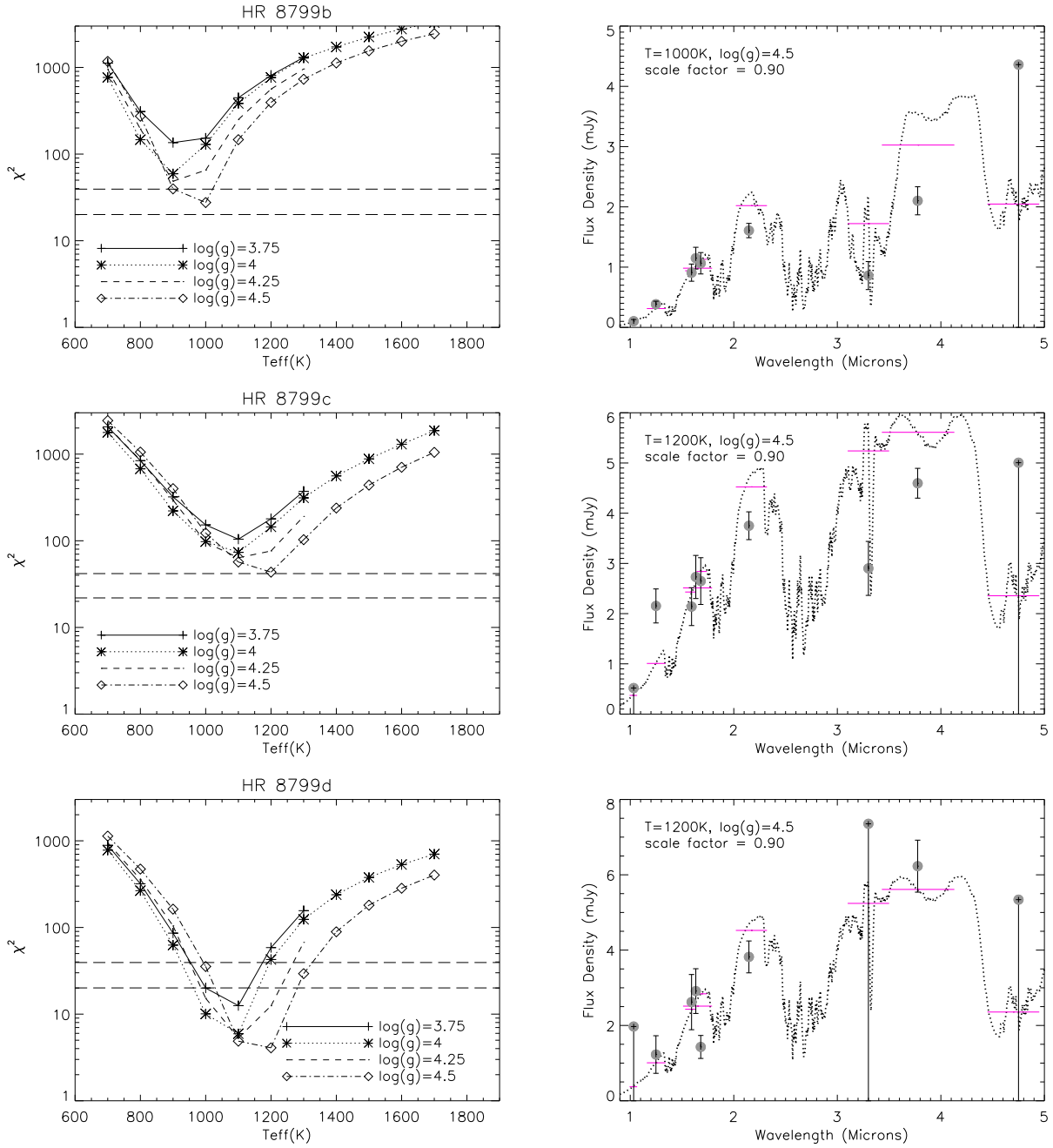

FIG. 12.— Same as Figure 11 except allowing the planet radius to depart by ± 10% from the Burrows et al. (1997) values.

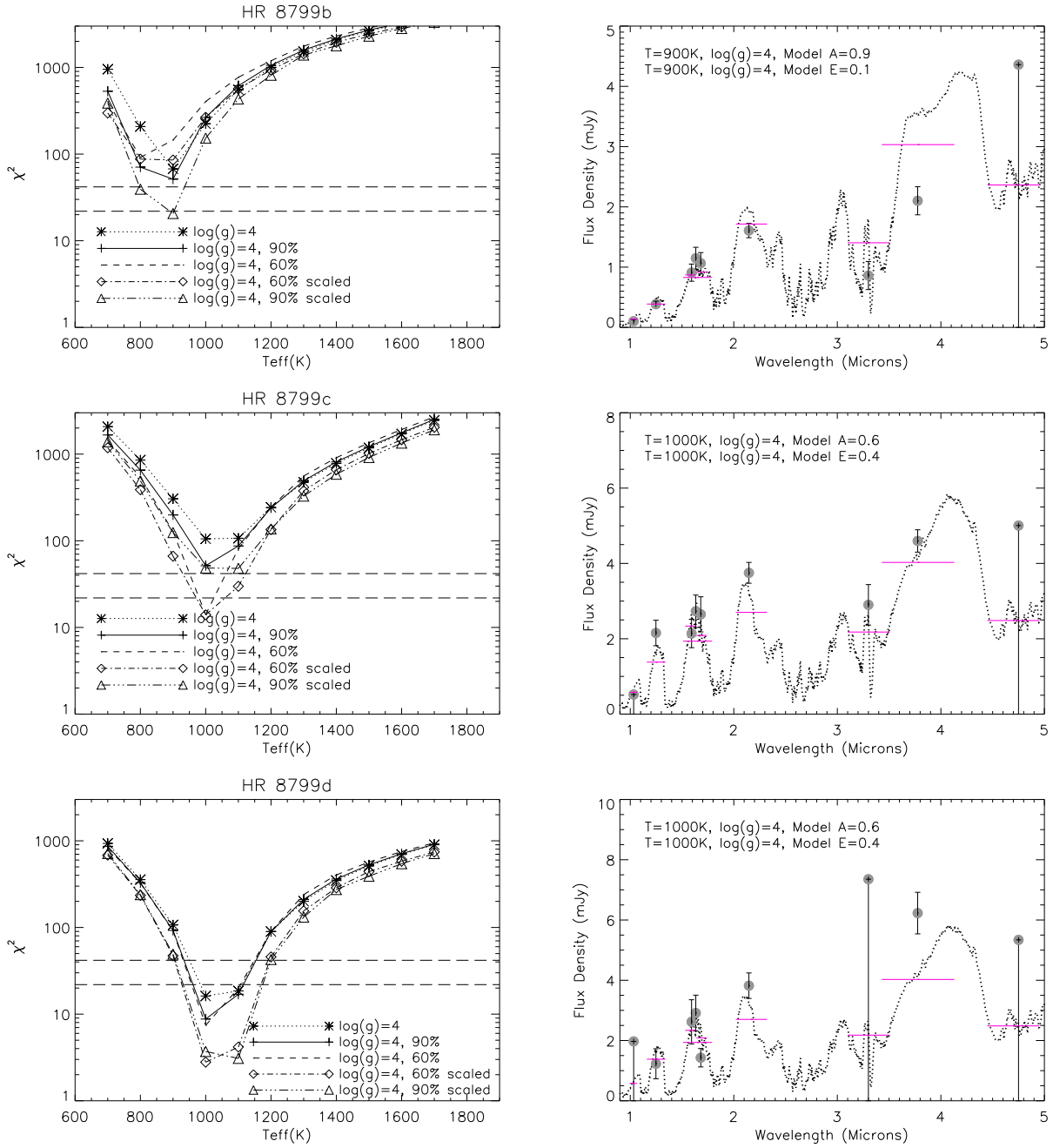

FIG. 13.— Fitting results for our simple approximation of a "patchy" cloud atmosphere. In all right-hand panels, the displayed best-fit SEDs have $C_k = 0.9$.

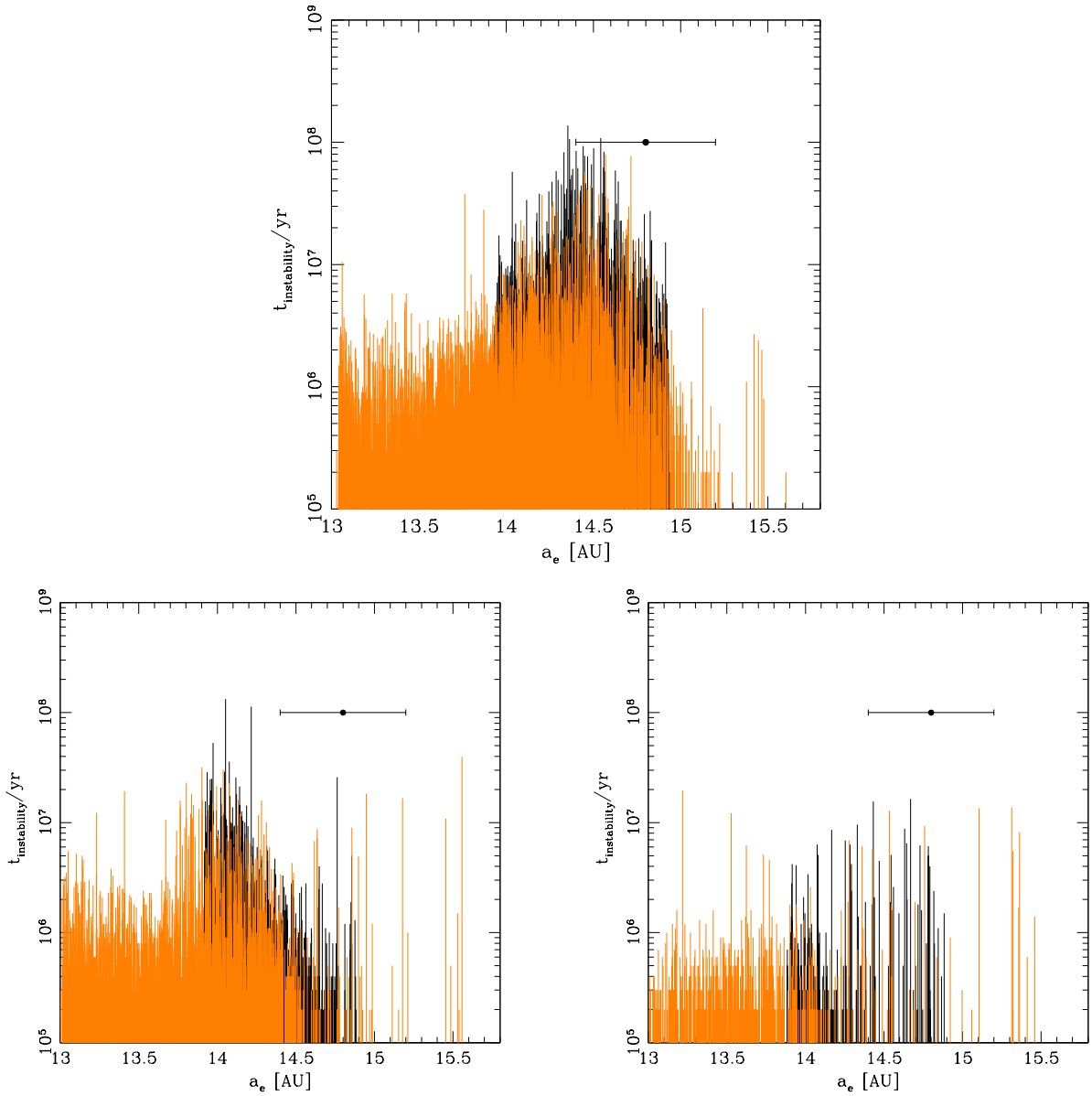

FIG. 14.— The time to dynamical instability vs. semimajor axis of HR 8799e for three separate sets of masses and orbital resonances. In all plots, the orange lines denote our set of simulations allowing HR 8799e to vary between 13.1 AU and 15.7 AU, while the black lines denote our simulations that restrict HR 8799e to be between 14 and 15 AU while more finely sampling the range of other orbital parameters (e.g. mean anomaly, longitude of periastron). The horizontal dot with error bars identifies the 1-σ range of projected separations for HR 8799e from our work. In Case A (top panel), HR 8799bcde have masses of 5, 7, 7, and 7 M_J. Case B (bottom-left) corresponds to planet masses of 7, 10, 10, and 10 M_J and Case C (bottom-right) correspond to 10, 13, 13, and 13 M_J. The density of the bars appears anomalously low for Case C because many simulations have instability times less than 10^5 years.

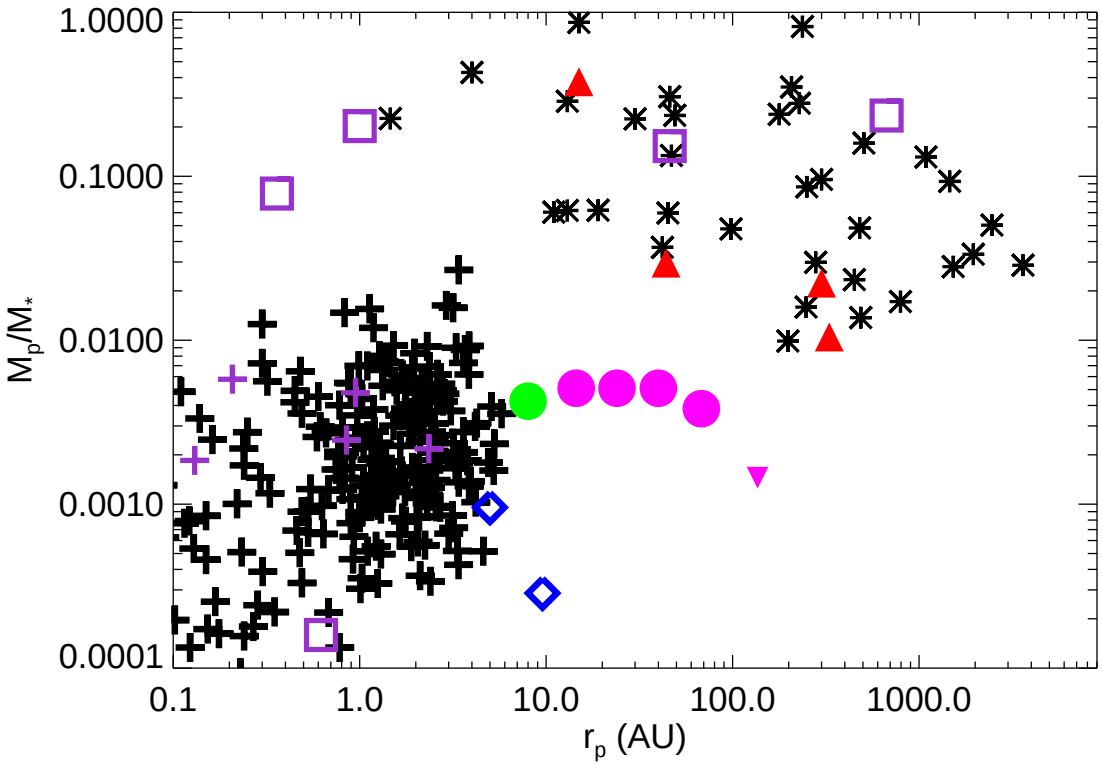

FIG. 15.— Updated version of the mass ratio vs. orbital separation plot from Kratter et al. (2010) incorporating our revised masses for HR 8799bcd (magenta dots). We also include HR 8799e, assigned a mass of 7 M_J from Marois et al. (2011), and displayed as the left-most magenta dot. The β Pic planet is specifically identified as a green dot (Lagrange et al. 2010). Fomalhaut b is a downward-pointing magenta triangle (Kalas et al. 2008; Chiang et al. 2009). Substellar companions discovered after or not included in the Kratter et al. (2010) publication – 1RXJS1609.1-210524, GJ 758B, 2M J044144b, and GSC 06214-00210B – are plotted as red triangles. Black crosses, purple crosses and purple squares denote radial velocity, transit, and microlensing-detected planets around stars with three mass bins: $M_\star \geq 0.4$ $M_\odot$, $M_\odot = 0.1$–0.4 $M_\odot$, and $M_\star < 0.1$ $M_\odot$. For direct comparisons and simplicity, we plot same the population of exoplanets *not* detected by direct imaging as that used Kratter et al. (2010) (e.g. we do not include planets discovered by RV or transits since the publication of this paper). Black asterisks denote the sample of substellar companions listed in Zuckerman and Song (2009). Jupiter and Saturn are plotted as blue diamonds.